Sensitivity of Inherent Optical Properties From Ocean Reflectance Inversion Models to Satellite Instrument Wavelength Suites

P. Jeremy Werdell[1*] and Lachlan I. W. McKinna[1,2]

[1] Ocean Ecology Laboratory, NASA Goddard Space Flight Center, Greenbelt, MD, United States, [2] Go2Q Pty Ltd., Buderim, QLD, Australia

The Earth science community seeks to develop climate data records (CDRs) from satellite measurements of ocean color, a continuous data record that now exceeds 20 years. Space agencies will launch additional instruments in the coming decade that will continue this data record, including the NASA PACE spectrometer. Inherent optical properties (IOPs) quantitatively describe the absorbing and scattering constituents of seawater and can be estimated from satellite-observed spectroradiometric data using semi-analytical algorithms (SAAs). SAAs exploit the contrasting optical signatures of constituent matter at spectral bands observed by satellite sensors. SAA performance, therefore, depends on the spectral resolution of the satellite spectroradiometer. A CDR spanning SeaWiFS, MODIS, OLCI, and PACE, for example, would include IOPs derived using varied wavelength suites if all available wavelengths were considered. Here, we explored differences in derived IOPs that stem simply from the use of (eight) different wavelength suites of input radiometric measurements. Using synthesized data and SeaWiFS Level-3 mission-long composites, we demonstrated equivalent SAA performance for all wavelength suites, but that IOP retrievals vary by several percent across wavelength suites and as a function of water type. The differences equate to roughly $\leq$ 6, 12, and 7% for $a_{dg}(443)$, $a_{ph}(443)$, and $b_{bp}(443)$, respectively, for waters with $C_a \leq 1$ mg m^{-3}. These values shrink for sensors with similar wavelength suites (e.g., SeaWiFS, MODIS, and MERIS) and rise to substantially larger values for higher C_a waters. Our results also indicate that including 400 nm (in the case of OLCI) influences the derived IOPs, using longer wavelengths (>600 nm) influences the derived IOPs when there is a red signal, and, including additional spectral information shows potential for improved IOP estimation, but not without revisiting SAA parameterizations and execution. While modest in scope, we believe this study contributes to the knowledge base for CDR development. The implication of ignoring such an analysis as CDRs continue to be developed is a prolonged inability to distinguish between algorithmic and environmental contributions to trends and anomalies in the IOP time-series.

Keywords: ocean color satellites, ocean remote sensing, bio-optics, semi-analytic inversion algorithms, inherent optical properties, remote-sensing reflectance

INTRODUCTION

The oceanographic community seeks to develop biogeochemical climate data records (CDRs) from satellite measurements of ocean color (NRC, 2011). The U.S. National Research Council defines a CDR as "a time series of measurements of sufficient length, consistency, and continuity to determine climate variability and change" (NRC, 2004). The continuous global data record from ocean color satellites now exceeds 20 years, including (but not limited to) the following instruments: the NASA Sea-viewing Wide Field of View Sensor (SeaWiFS; 1997–2010), the NASA Moderate Resolution Imaging Spectroradiometers (MODIS; 1999-present onboard Terra and 2002-present onboard Aqua), the ESA Medium Resolution Imaging Spectrometer (MERIS; 2002–2012), the Visible Infrared Imaging Radiometer Suite (VIIRS; 2012-present onboard Suomi NPP and 2018-present onboard JPSS-1), the ESA Ocean and Land Color Instrument (OLCI; 2016-present onboard Sentinel-3A and 2018-present onboard Sentinel-3B), and the JAXA Second generation GLobal Imager (SGLI; 2017-present). NASA and several international space agencies plan to launch additional ocean color instruments in the coming decade, including the NASA Plankton, Aerosol, Cloud, ocean Ecosystem (PACE; 2022 launch) ocean color instrument. To facilitate CDR development, the community invests substantially into ensuring the characterization of the space-borne radiometric measurements (e.g., Meister et al., 2012; Zibordi et al., 2014; Meister and Franz, 2014) and the consistency of their derived data products (e.g., Franz et al., 2005; Werdell et al., 2009; Melin and Sclep, 2015; Barnes and Hu, 2016; Mélin et al., 2016). Sathyendranath et al. (2017) provides a useful exploration of desired characteristics of satellite-derived ocean color products for CDR development, including, and perhaps more importantly, analyses to support discussion of the implications potentially realized when these characteristics are not met.

Ocean color satellite instruments provide estimates of spectral remote-sensing reflectance [$R_{rs}(\lambda)$; sr^{-1}], the light exiting the water normalized to the hypothetical condition of a non-attenuating atmosphere with an overhead Sun, after atmospheric correction (Mobley et al., 2016). Bio-optical algorithms are applied to the $R_{rs}(\lambda)$ to produce estimates of geophysical and optical quantities, such as the near surface concentration of the phytoplankton pigment chlorophyll-a (C_a; mg m^{-3}) (O'Reilly et al., 1998) and spectral marine inherent optical properties (IOPs) (Werdell et al., 2018). Time-series of remotely-sensed IOPs provide valuable data records for studying long-term changes in ocean ecosystems. IOPs, the spectral absorption and scattering properties of seawater and its particulate and dissolved constituents, can be used to infer the contents of the upper ocean. This information is critical for advancing our understanding of biogeochemical oceanic processes such as carbon exchanges and fluxes, phytoplankton community dynamics, and ecosystem responses to disturbances (e.g., Behrenfeld et al., 2005; IOCCG, 2009, 2014, 2018; Siegel et al., 2014).

Semi-analytical algorithms (SAAs) provide one mechanism for estimating marine IOPs from $R_{rs}(\lambda)$ using a combination of empiricism and radiative transfer theory (Werdell et al., 2018). Most SAAs attempt to simultaneously estimate the magnitudes of spectral backscattering by particles [$b_{bp}(\lambda)$; m^{-1}], absorption by phytoplankton [$a_{ph}(\lambda)$; m^{-1}], and the combined absorption by non-algal particles and colored dissolved organic material [$a_{dg}(\lambda)$; m^{-1}]. This is typically accomplished by assigning constant spectral values for seawater absorption and backscattering, assuming spectral shape functions for the remaining constituent absorption and scattering components, and retrieving the magnitudes of each remaining constituent required to match the spectral distribution of $R_{rs}(\lambda)$. Such spectral-matching algorithms require contrasting optical signatures for $a_{dg}(\lambda)$, $a_{ph}(\lambda)$, and $b_{bp}(\lambda)$ within the spectral bands detected by the satellite. The performance of most SAAs therefore depends on the spectral resolution of $R_{rs}(\lambda)$ used as input to the algorithm, which is primarily driven by the spectral resolution of the satellite radiometer (Lee et al., 2007; Werdell et al., 2014; Wolanin et al., 2016; Vandermuelen et al., 2017). Conventional wisdom now supports the inclusion of additional ultraviolet-visible wavelengths into new satellite radiometers (relative to historical instruments such as SeaWiFS) to enable the improved discrimination of particulate and dissolved components within seawater and of absorbing and non-absorbing atmospheric aerosols (PACE Science Definition Team, 2018).

Semi-analytical algorithms continue to evolve rapidly, and substantial focus has been placed on intercomparisons (IOCCG, 2006; Brewin et al., 2015), reducing the number of required assumptions [e.g., Zheng and Stramski, 2013; and estimation of uncertainties (Werdell et al., 2018) and references therein]. Uncertainties in SAA-derived IOPs arise from multiple sources: uncertainties in input $R_{rs}(\lambda)$ (Maritorena et al., 2010), assumptions embedded into the adopted $R_{rs}(\lambda)$-to-IOPs relationship (Lee et al., 2004, 2011), the choice of spectral-matching method [see Appendix A of Werdell et al. (2013a)], accounting (or not accounting) for inelastic scattering (Lee et al., 1994; Westberry et al., 2013; McKinna et al., 2016; Loisel et al., 2018), the ancillary data sources used for various corrections (Werdell et al., 2013b), and the assignment of spectral shape functions for $a_{dg}(\lambda)$, $a_{ph}(\lambda)$, and $b_{bp}(\lambda)$ to name only a few. With regards to the latter, for example, any single spectrum cannot unequivocally represent all water masses at all times and Werdell et al. (2013a) demonstrated that selecting alternate spectral shapes can vary derived IOPs by up to ~100%. Note also that most SAAs do not currently include account for the polarization of light (Ibrahim et al., 2012; Gilerson et al., 2014).

In concert with this ongoing refinement, time-series of data products from SAAs continue to be developed, with the larger goal of producing CDRs (Behrenfeld et al., 2005; Siegel et al., 2013). Some focus has been placed on merging satellite IOP data records (Maritorena et al., 2010), but fewer studies have explored differences in derived products that stem simply from the use of different suites of input $R_{rs}(\lambda)$. For example, SeaWiFS had a green wavelength centered on 510 nm, whereas the MODIS instruments' green wavelength is centered on 531 nm and VIIRS does not include a green wavelength. A CDR from

these instruments spanning 1997 to present would therefore include IOPs derived using varied wavelength suites if all available wavelengths were considered. It remains conceivable that different combinations of input $R_{rs}(\lambda)$ yield differences in IOPs that exceed the magnitude of observable environmental change in a CDR. Albeit modest in scope, the goal of this paper is simply to use a controlled modeling environment to quantify the magnitude of change in derived IOPs associated with the use of different spectral suites of satellite $R_{rs}(\lambda)$. The implication of ignoring such an analysis as CDRs continue to be developed is a prolonged inability to distinguish between algorithmic and environmental contributions to trends and anomalies in the IOP time-series.

METHODS

Data Acquisition

For the sensitivity analyses, we generated a synthesized dataset of coincident $R_{rs}(\lambda)$, $a_{dg}(\lambda)$, $a_{ph}(\lambda)$, $b_{bp}(\lambda)$, and C_a that closely mimics the IOCCG Ocean Color Algorithms Working Group synthetic dataset (IOCCG, 2006), but with expanded and finer spectral resolution. Appendix A describes its development (see the online article page to access the **Appendix**). This dataset maintains a spectral resolution of 1 nm intervals from 350 to 800 nm. We targeted $R_{rs}(\lambda)$ and IOPs at the following center satellite wavelengths:

- SeaWiFS: 412, 443, 490, 510, 555, 670
- MODIS: 412, 443, 488, 531, 547, 667
- MERIS: 412, 443, 490, 510, 560, 620, 665
- VIIRS: 410, 443, 486, 551, 671
- OLCI: 400, 412, 443, 490, 510, 560, 620, 665
- PACE: 400, 412, 425, 443, 460, 475, 490, 510, 532, 555, 583, 617, 640, 655, 665
- 410–670 nm: 5 nm intervals from 410 to 670 nm
- 410–600 nm: 5 nm intervals from 410 to 600 nm

The latter three wavelength suites all represent possibilities for PACE, with the first of these three (15 wavelengths) indicating aggregated bands to be distributed by the mission (PACE Science Definition Team, 2018) and the second and third representing the full science resolution of the spectrometer (5 nm) spanning two ranges for inversion (410–600 nm vs. 410–670 nm). While it remains tempting to execute the inversion using the full spectrum of the synthesized dataset, we opted to limit our 5 nm examples to a SeaWiFS-like range to specifically compare differences in performance when using contiguous (so called hyperspectral) spectra vs. discrete heritage wavelengths. Furthermore, we feel the extension of SAA inversions into the ultraviolet remains sufficiently underdeveloped to warrant examination in separate works. We explored a more limited hyperspectral range—to only 600 nm in lieu of 670 nm—to evaluate the impact of very low red radiometric signals in the inversion. For comparative purposes with heritage instruments, we also estimated IOP retrievals for the two 5 nm cases (410–670 and 410–600 nm) at 443 nm using a cubic spline fit on the retrieved $a_{dg}(\lambda)$, $a_{ph}(\lambda)$, and $b_{bp}(\lambda)$.

The native synthesized dataset defines its IOPs using four orders of magnitude of C_a (20 values within the range 0.03 to

30 mg m^{-3}, $N = 500$) (IOCCG, 2006). In most cases (specifically noted), we limited our analyses to $0.03 \leq C_a \leq 5$ mg m^{-3}, as the SAA became sufficiently unstable from instrument-to-instrument above 5 mg m^{-3} such that low retrieval sample sizes confounded meaningful reporting of results ($N \cong 350$). We discuss the strengths and weaknesses of these synthesized data for our analyses in section Discussion. For the satellite comparisons, we acquired the mission-mean (1997–2010) SeaWiFS Level-3 $R_{rs}(\lambda)$ bin file at 9 km spatial resolution from the NASA Ocean Biology Processing Group (OBPG; https://oceancolor.gsfc.nasa.gov; reprocessing version 2018.0). For several analyses, we stratified the results into three C_a ranges—$C_a \leq 0.1$ mg m^{-3} (intended to represent oligotrophic water), $0.1 < C_a \leq 1$ mg m^{-3} (mesotrophic), and $C_a > 1$ mg m^{-3} (eutrophic)—to broadly evaluate performance differences as a function of water type. We note that shape and magnitude of synthesized $R_{rs}(\lambda)$ spectra shift from being blue-dominated to red-dominated as the water type transitions from oligotrophic to eutrophic as shown in **Figure 1**.

Regarding our use of single center wavelengths for this exercise, we acknowledge that different satellite instruments maintain inherently different radiometric bandpasses. Standard NASA processing applies an out-of-band correction using instrument-specific spectral response functions that adjusts the retrieved $R_{rs}(\lambda)$ to the nominal band centers after atmospheric correction (Wang et al., 2001; Patt et al., 2003). Given that this is done prior to execution of an SAA, our use of center wavelengths sufficiently mimics the satellite input $R_{rs}(\lambda)$—acknowledging, of course, that the out-of-band adjustment carries uncertainties that inevitably impact the final IOP retrievals.

Inversion Modeling

Our default SAA adopts the default generalized IOP (GIOP) form described in Werdell et al. (2013a). Briefly, $R_{rs}(\lambda)$ are first converted to their subsurface values following (Lee et al., 2002):

$$r_{rs}\left(\lambda, 0^-\right) = \frac{R_{rs}\left(\lambda\right)}{0.52 + 1.7\, R_{rs}\left(\lambda\right)}. \qquad (1)$$

Subsurface remote-sensing reflectances relate to marine IOPs following (Gordon et al., 1988):

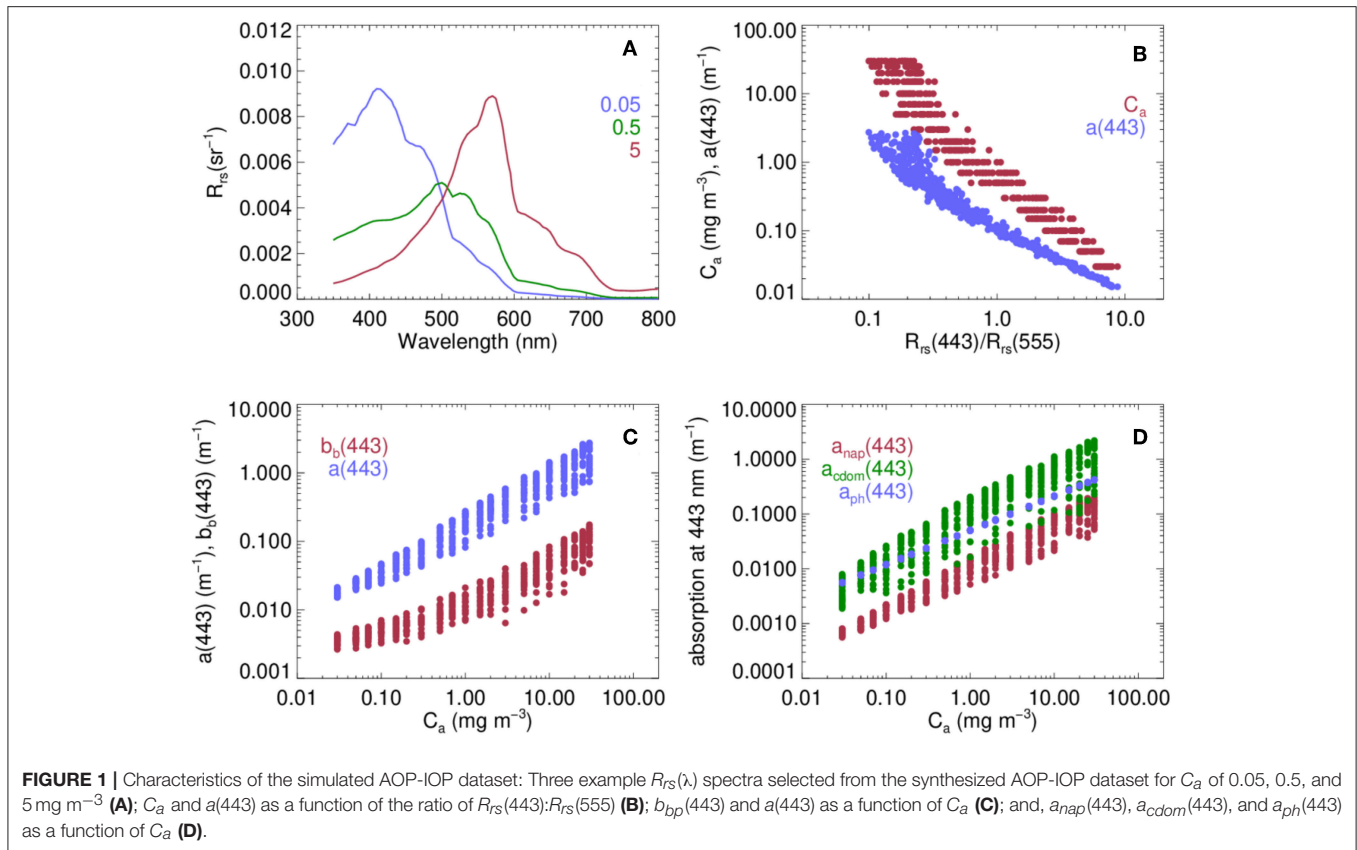$$r_{rs}\left(\lambda, 0^-\right) = 0.0949\, u + 0.0794\, u^2, \qquad (2a)$$

$$u(\lambda) = \frac{b_b\left(\lambda\right)}{a\left(\lambda\right) + b_b\left(\lambda\right)} \qquad (2b)$$

where $b_b(\lambda)$ is the total backscattering coefficient (m^{-1}) and $a(\lambda)$ is the total absorption coefficient (m^{-1}). Total backscattering can be expanded as the sum of all backscattering components. Further, each component can be expressed as the product of its mass-specific backscattering spectrum (spectral shape; b^*) and its magnitude or concentration (M):

$$b_b\left(\lambda\right) = b_{bw}\left(\lambda\right) + M_{bp}\, b_{bp}^*(\lambda). \qquad (3)$$

Similarly, total absorption can be expanded to:

$$a\left(\lambda\right) = a_w\left(\lambda\right) + M_{dg} a_{dg}^*\left(\lambda\right) + M_{ph} a_{ph}^*\left(\lambda\right). \qquad (4)$$

FIGURE 1 | Characteristics of the simulated AOP-IOP dataset: Three example $R_{rs}(\lambda)$ spectra selected from the synthesized AOP-IOP dataset for C_a of 0.05, 0.5, and 5 mg m^{-3} **(A)**; C_a and $a(443)$ as a function of the ratio of $R_{rs}(443):R_{rs}(555)$ **(B)**; $b_{bp}(443)$ and $a(443)$ as a function of C_a **(C)**; and, $a_{nap}(443)$, $a_{cdom}(443)$, and $a_{ph}(443)$ as a function of C_a **(D)**.

where the subscript w indicates contributions by water. Both $b_{bw}(\lambda)$ and $a_w(\lambda)$ are known (Pope and Fry, 1997; Zhang et al., 2009). Werdell et al. (2013a) describes in the detail the rationale for the default choices of $b_{bp}^*(\lambda)$, $a_{dg}^*(\lambda)$, and $a_{ph}^*(\lambda)$. By default, we expressed $b_{bp}^*(\lambda)$ as $\lambda^{S_{bp}}$, where S_{bp} defines the steepness of the power law and typically varies between -2 and 0 in natural waters (Stramski et al., 2004). We dynamically assigned S_{bp} to each station/pixel using the $R_{rs}(\lambda)$ band-ratio method described in Lee et al. (2002). We expressed $a_{dg}^*(\lambda)$ as exp(-S_{dg} λ), where S_{dg} describes the rate of exponential decay and typically varies between 0.01 and 0.02 nm^{-1} (Roesler et al., 1989), and adopted a fixed S_{dg} of 0.018 nm^{-1}. Finally, we expressed $a_{ph}^*(\lambda)$ as the C_a-specific absorption spectrum of Bricaud et al. (1998) seeded using each station/pixel-specific C_a and normalized to 0.055 m^2 mg^{-1} at 443 nm. Broadly speaking, many alternatives for such parameterizations exist (as explored in Werdell et al., 2013a), but our choices in parameterization remain of secondary importance for this paper given that we apply them consistently across analyses.

Three unknowns remain in Equations (1–4) after assignment of the eigenvectors, namely M_{bp}, M_{dg}, and M_{ph}. Using $R_{rs}(\lambda)$ as input, the SAA estimates these eigenvalues via non-linear least squares (Levenberg-Marquardt) inversion of Equation (2) with minimization of a χ^2 cost function [see Equation (11) of Werdell et al., 2013a]. We retained only those solutions with viable estimates of M_{bp}, M_{dg}, and M_{ph} [for example, -0.005

$\leq a_{dg}(\lambda) \leq 5$ m^{-1}] that resulted in reconstructed $R_{rs}(\lambda)$ that differed from the input $R_{rs}(\lambda)$ by $< 33\%$ in the range 400 to 600 nm. We reconstructed $R_{rs}(\lambda)$ using the retrieved eigenvalues as input into Equations (1–4) and defined failure as non-convergence in the inversion. Werdell et al. (2013a) outlines exclusion criteria used to determine viable estimates, as well as the similarities in accuracy shared by this SAA configuration and other common approaches.

Analyses

We ran the inversion model using the synthesized $R_{rs}(\lambda)$ for every satellite input wavelength suite listed in section Data Acquisition. We then statistically compared the model-derived IOPs (hereafter referred to by satellite to identify the input wavelength suite) with the source synthesized IOPs. Our reported statistics include the sample size (N), the Type I linear regression slope, the median absolute error (MAE), and the bias. We calculated MAE as:

$$MAE = 10 \wedge \left(\frac{\sum_{i=1}^{N} \left| \log_{10}\left(satellite_i\right) - \log_{10}\left(synthesized_i\right) \right|}{N} \right) \quad (5)$$

and bias as:

$$bias = 10 \wedge \left(\frac{\sum_{i=1}^{N} \log_{10}\left(satellite_i\right) - \log_{10}\left(synthesized_i\right)}{N} \right) . \quad (6)$$

TABLE 1 | Statistics for SAA-derived vs. synthesized IOPs at 443 nm.

		Bias	MAE	Slope
SeaWiFS	a	1.08	1.10	1.07
$N = 356$	a_{dg}	0.93	1.27	1.03
	a_{ph}	1.24	1.50	1.05
	b_{bp}	1.10	1.15	1.01
MODIS	a	1.07	1.09	1.05
$N = 335$	a_{dg}	0.92	1.27	1.03
	a_{ph}	1.17	1.51	0.92
	b_{bp}	1.08	1.14	0.99
MERIS	a	1.04	1.06	1.02
$N = 354$	a_{dg}	0.91	1.26	1.01
	a_{ph}	1.14	1.47	0.92
	b_{bp}	1.05	1.12	0.96
VIIRS	a	1.07	1.10	1.06
$N = 345$	a_{dg}	0.91	1.27	1.03
	a_{ph}	1.24	1.52	0.99
	b_{bp}	1.09	1.16	0.99
OLCI	a	1.04	1.07	1.02
$N = 364$	a_{dg}	0.89	1.26	1.01
	a_{ph}	1.23	1.48	0.97
	b_{bp}	1.07	1.13	0.97
PACE	a	1.03	1.05	1.01
$N = 343$	a_{dg}	0.89	1.25	1.00
	a_{ph}	1.11	1.54	0.85
	b_{bp}	1.05	1.12	0.94
410–670 nm	a	0.98	1.05	1.00
$N = 332$	a_{dg}	0.85	1.27	1.00
	a_{ph}	1.00	1.53	0.84
	b_{bp}	1.01	1.10	0.94
410–600 nm	a	0.98	1.05	1.01
$N = 347$	a_{dg}	0.86	1.27	1.01
	a_{ph}	1.04	1.50	0.87
	b_{bp}	1.01	1.10	0.94

Note that observations are log-transformed such that MAE and bias present multiplicative metrics (that is, a MAE of 1.5 indicates that the satellite observations are $1.5 \times$ (50% greater) on average than the synthesized observations and a bias less than unity indicates a negative bias). Note also that **Table 1** reports bias and MAE as calculated in Equations (5) and (6), but we discuss these performance metrics using their more intuitive percentage counterparts throughout the Results and Discussion sections.

Next, we compared derived IOPs from each satellite wavelength suite with those from every other satellite wavelength suite. This comparison included determination of unbiased percent differences (UPD). We calculated UPD for two satellites (satellite$_1$ and satellite$_2$) as:

$$UPD = 200\% \left(\frac{satellite_2 - satellite_1}{satellite_2 + satellite_1} \right) \quad (7)$$

and report the median UPD for the complete population of match-ups. A negative UPD indicates that the IOP from satellite$_2$ is biased low relative to satellite$_1$.
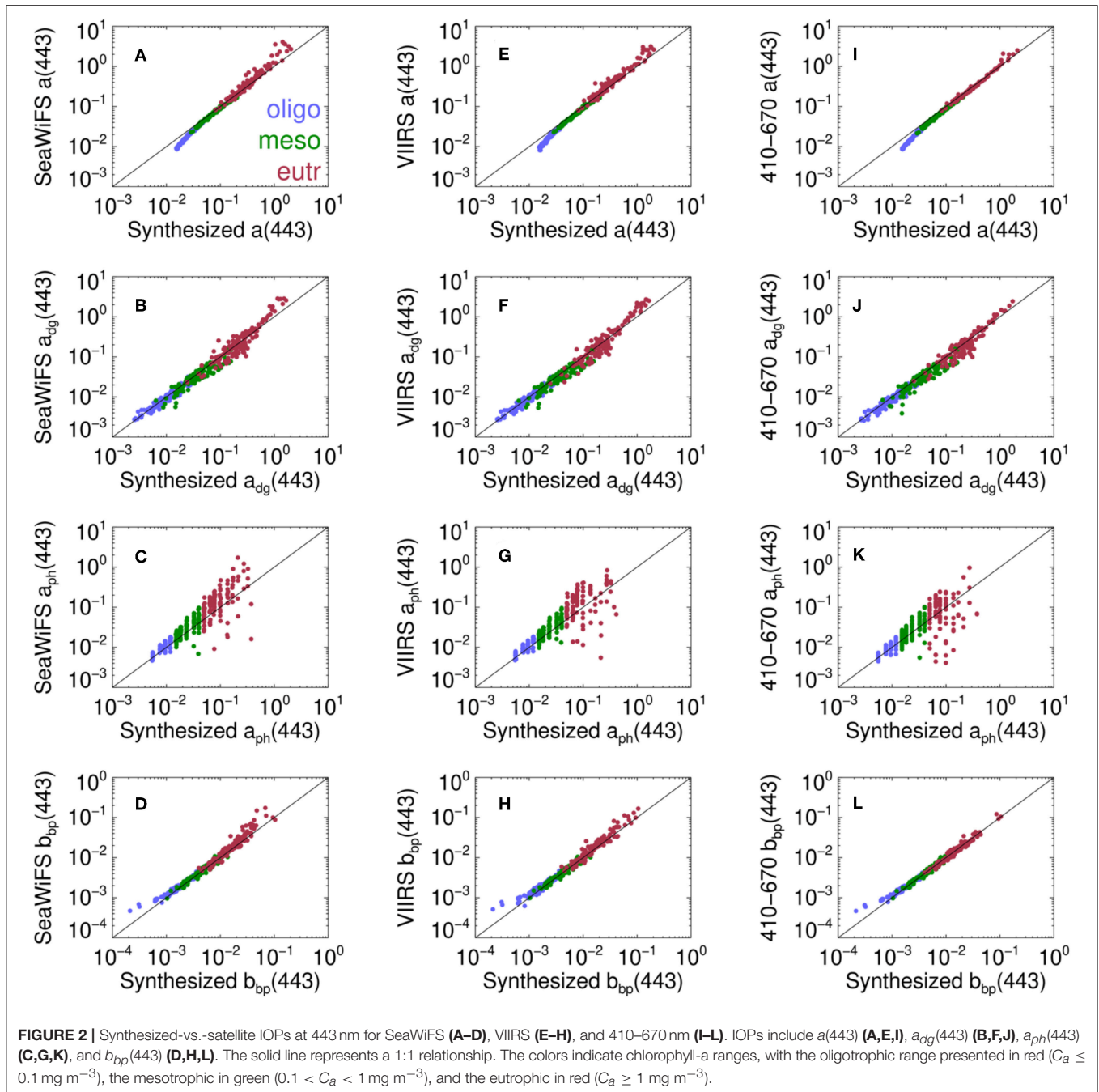
To evaluate if the results varied with the configuration of the inversion model (that is, if they varied with assignment of spectral shapes), we ran the inversion model for each satellite input $R_{rs}(\lambda)$ wavelength suite an additional seven times, sequentially re-assigning one variable per run as: (1) default S_{bp} from Lee et al. (2002) + 33%; (2) default S_{bp} from Lee et al. (2002) −33%; (3) default S_{dg} + 33% (= 0.024 nm^{-1}); (4) default S_{dg} −33% (= 0.012 nm^{-1}); (5) seed C_a to calculate $a_{ph}^*(\lambda)$ using Bricaud et al. (1998) + 50%; (6) seed C_a to calculate $a_{ph}^*(\lambda)$ using Bricaud et al. (1998) −50%; and, (7) replacing 0.0949 and 0.0794 in Equation (2a) with 0.0895 and 0.1247 as in Lee et al. (2002).

Finally, we twice ran the default inversion model (as defined in section Inversion Modeling) on the mission-long mean Level-3 SeaWiFS $R_{rs}(\lambda)$ to determine if results from our controlled modeling environment were generally representative of real satellite data. To do so, we used OBPG-supported satellite data processing software (l3 gen) to run the inversion model via the GIOP software framework, which allows assignment of wavelengths to be used in the inversion, on the Level-3 SeaWIFS $R_{rs}(\lambda)$. The NASA SeaWiFS Data Analysis Software (SeaDAS; https://seadas.gsfc.nasa.gov) package includes this software. The first run used all six SeaWiFS wavelengths. The second run served to mimic VIIRS and, as such, we only assigned the five common SeaWiFS-VIIRS wavelengths. Given the known differences between SeaWiFS and VIIRS $R_{rs}(\lambda)$ (Eplee et al., 2015; Barnes and Hu, 2016), using a narrower SeaWiFS band set as a surrogate for VIIRS provided a more suitable controlled environment to explore differences in band selection.
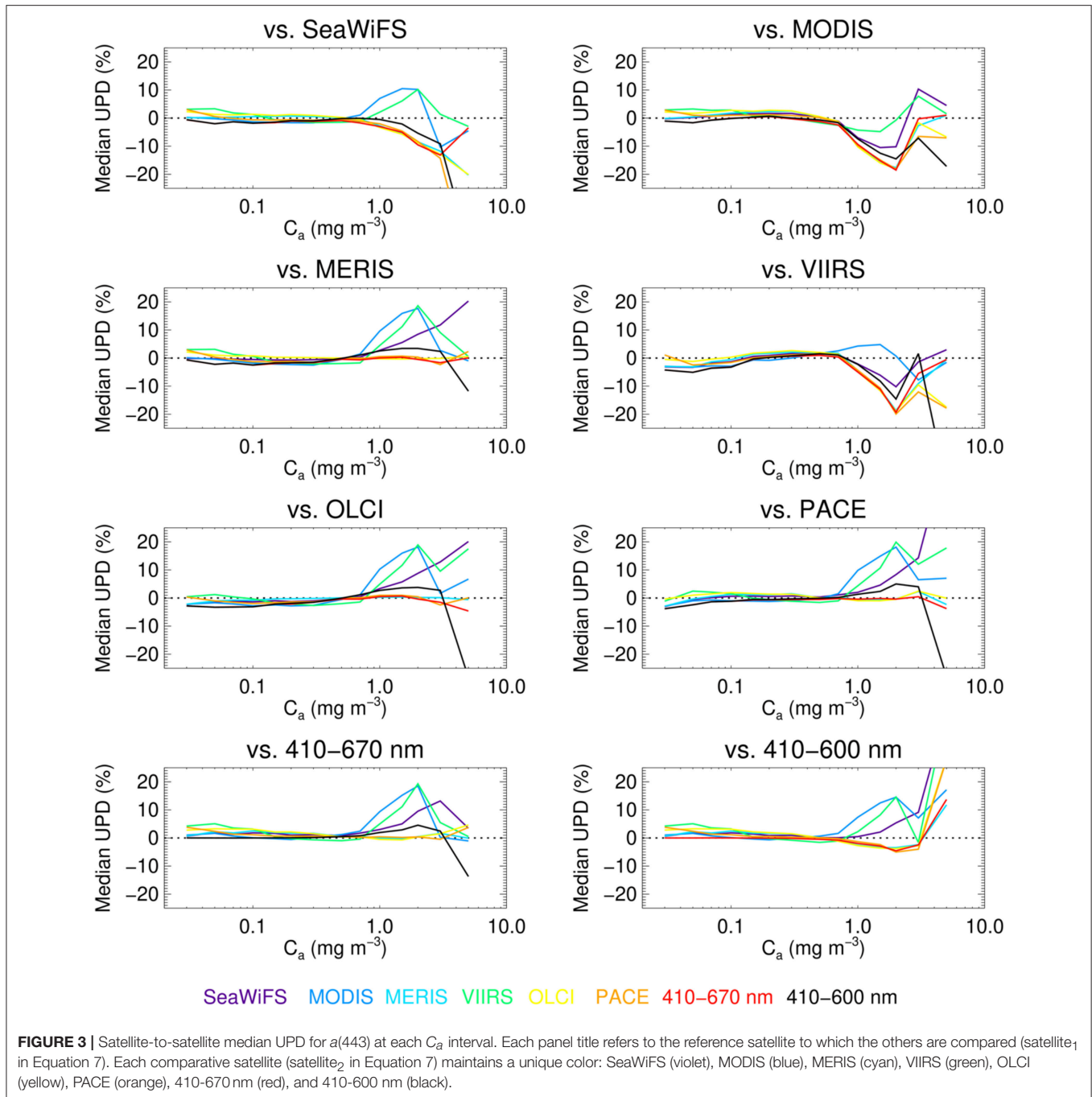
RESULTS

Data Product Validation

Broadly speaking, the satellite-to-synthesized IOP validation analyses demonstrated equivalent performance across all wavelength suites (**Figure 2**, **Table 1**), with performance metrics that mirror those from previous studies that used equivalent simulated datasets (e.g., IOCCG, 2006; Lee et al., 2010; Werdell et al., 2013a). All runs reported very similar MAE, ranging from 5 to 10% for $a(443)$ and 10 to 16% for $b_{bp}(443)$ and from 5 to 8% for $a(555)$ and 8 to 14% for $b_{bp}(555)$. In general, we achieved comparable results across blue-green wavelengths for all analyses and, thus, our tables and figures focus only on 443-nm for clarity in presentation of results. MAEs for the absorption subcomponents ranged from 25 to 27% for $a_{dg}(443)$ and 47 to 54% for $a_{ph}(443)$. Every wavelength suite carried its lowest MAEs for $a(443)$ and the highest MAE for $a_{ph}(443)$. The regression slopes behaved similarly. All runs reported very similar values for $a(\lambda)$, $a_{dg}(\lambda)$, and $b_{bp}(\lambda)$, ranging from 1.00 to 1.07 for $a(443)$, 1.03 to 1.06 for $a_{dg}(443)$ and 0.94 to 1.01 for $b_{bp}(443)$. Across IOPs for each wavelength suite, $a_{ph}(443)$ deviated most substantially from unity. It also exhibited the broadest range across wavelength suites, ranging from 0.72 to 1.05. Interestingly, the runs with the most

FIGURE 2 | Synthesized-vs.-satellite IOPs at 443 nm for SeaWiFS **(A–D)**, VIIRS **(E–H)**, and 410–670 nm **(I–L)**. IOPs include $a(443)$ **(A,E,I)**, $a_{dg}(443)$ **(B,F,J)**, $a_{ph}(443)$ **(C,G,K)**, and $b_{bp}(443)$ **(D,H,L)**. The solid line represents a 1:1 relationship. The colors indicate chlorophyll-a ranges, with the oligotrophic range presented in red ($C_a \leq$ 0.1 mg m^{-3}), the mesotrophic in green ($0.1 < C_a < 1$ mg m^{-3}), and the eutrophic in red ($C_a \geq 1$ mg m^{-3}).

wavelengths (PACE, 410–670 nm, and 410–600 nm) reported the $a_{ph}(443)$ regression slopes that deviated most from unity. The satellite-to-synthesized biases diverged more across runs than either MAE or regression slope. While $a(443)$ biases spanned across unity, all $a_{dg}(443)$ biases fell below unity (recall that a bias less than unity indicates a negative bias), ranging from 7% for SeaWiFS to 15% for the 410–670 nm run, and all $a_{ph}(443)$ biases fell either very close to unity or were positive, ranging from exactly unity for the 410–670 nm run to 24% for SeaWiFS and VIIRS. All $b_{bp}(443)$ biases exceeded unity

(were positive), ranging from 1% for the two 5 nm runs to 10% for SeaWiFS.

These results predominantly encompass simulations with $C_a \leq 5$ mg m^{-3}, as 85% of SAA failures occurred for those simulations with higher C_a values (reducing the viable N to $\cong 350$ as previously mentioned). Few failures resulted from non-convergence in the inversion. Rather, most occurred because of quality assurance metrics applied to the IOP retrievals, including requiring them to fall within predefined acceptable ranges (for example, $-0.005 \leq a_{dg}(\lambda) \leq 5$ m^{-1}) and requiring

FIGURE 3 | Satellite-to-satellite median UPD for a(443) at each C_a interval. Each panel title refers to the reference satellite to which the others are compared (satellite[1] in Equation 7). Each comparative satellite (satellite[2] in Equation 7) maintains a unique color: SeaWiFS (violet), MODIS (blue), MERIS (cyan), VIIRS (green), OLCI (yellow), PACE (orange), 410-670 nm (red), and 410-600 nm (black).

that reconstructed $R_{rs}(\lambda)$ differ from input $R_{rs}(\lambda)$ by < 33% at every wavelength in the range 400 to 600 nm. While relaxing or modifying these quality assurance metrics would enable extending our analyses into more complex water, we opted to not do so to: (a) ensure that our results encompassed only the highest quality SAA retrievals; (b) limit the introduction of results biases that emerge from global SAA parameterizations that do not properly represent complex waters; and, (c) acknowledge that the simulated dataset itself may be the least representative of natural conditions in this C_a range. Moreover, as simulations

with $C_a > 5$ mg m^{-3} realized so few results (low sample sizes), we opted to exclude them from subsequent analyses and data product intercomparisons. Follow-on analyses will benefit from additional attention to SAAs and datasets that better represent optically complex water.

Data Product Inter-comparisons

IOP retrievals for the synthetic dataset varied across wavelength suites and as a function of water type as defined by C_a (**Figures 3**–**6**, **Tables 2**–**4**). UPDs in a(443), a_{dg}(443), a_{ph}(443),

FIGURE 4 | As for **Figure 3**, but for $a_{dg}(443)$.
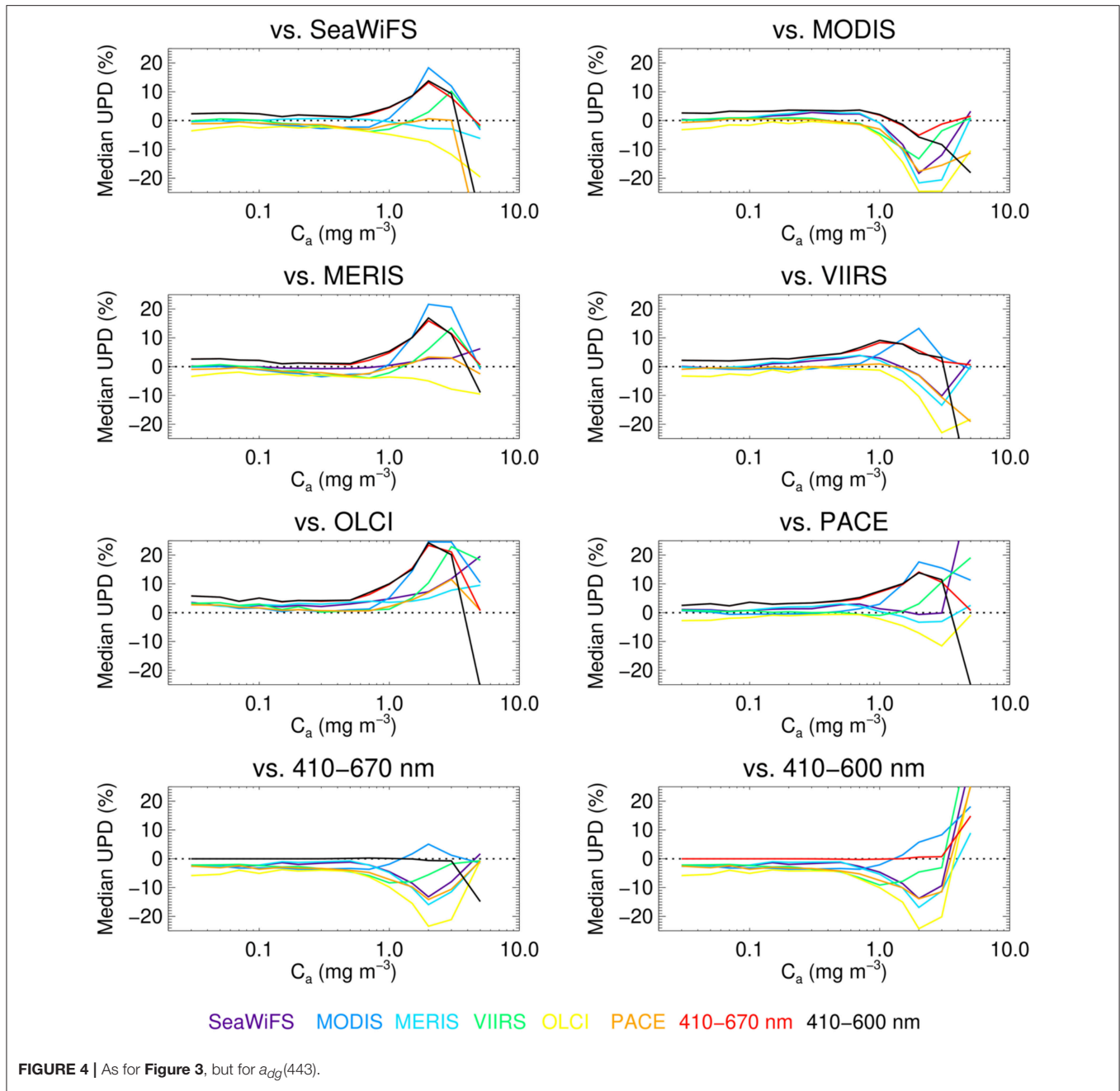
and $b_{bp}(443)$ across all wavelength suites ranged from -3.83 to 2.91%, -3.14 to 5.27%, -11.57 to 6.33%, and -6.09 to 4.74%, respectively, for the lowest C_a waters (**Table 2**). For comparison, UPDs in $a(555)$, $a_{dg}(555)$, $a_{ph}(555)$, and $b_{bp}(555)$ for SeaWiFS, PACE, and the two 5 nm wavelength suites (the only four suites with 555 nm) ranged from -0.51 to 0.35%, -0.74 to 3.13%, -6.65 to 1.47%, and -2.78 to 1.52%, respectively. Generally speaking, the differences between any two wavelength suites remained constant for all $C_a \leq 0.1\,\mathrm{mg\,m^{-3}}$ (**Figures 3–6**). Retrievals for the wavelength suites we consider most similar, SeaWiFS, MODIS, and MERIS, generally differed the least—by

≤ 0.92, 0.40, 1.11, and 1.25% for $a(443)$, $a_{dg}(443)$, $a_{ph}(443)$, and $b_{bp}(443)$, respectively, in absolute terms. OLCI retrieved low $a_{dg}(443)$ and high $a_{ph}(443)$ relative to all other wavelength suites, perhaps due to the inclusion of a 400 nm band that altered the separation of the two absorption subcomponents. The two 5 nm wavelength suites retrieved high $a_{dg}(443)$, low $a_{ph}(443)$, and low $b_{bp}(443)$ relative to all other wavelength suites. With only several exceptions, they also realized the highest magnitude UPDs.

For the mesotrophic C_a range, UPDs in $a(443)$, $a_{dg}(443)$, $a_{ph}(443)$, and $b_{bp}(443)$ across all wavelength suites ranged from -1.66 to 1.80%, -3.18 to 4.79%, -10.46 to 4.50%, and -2.27

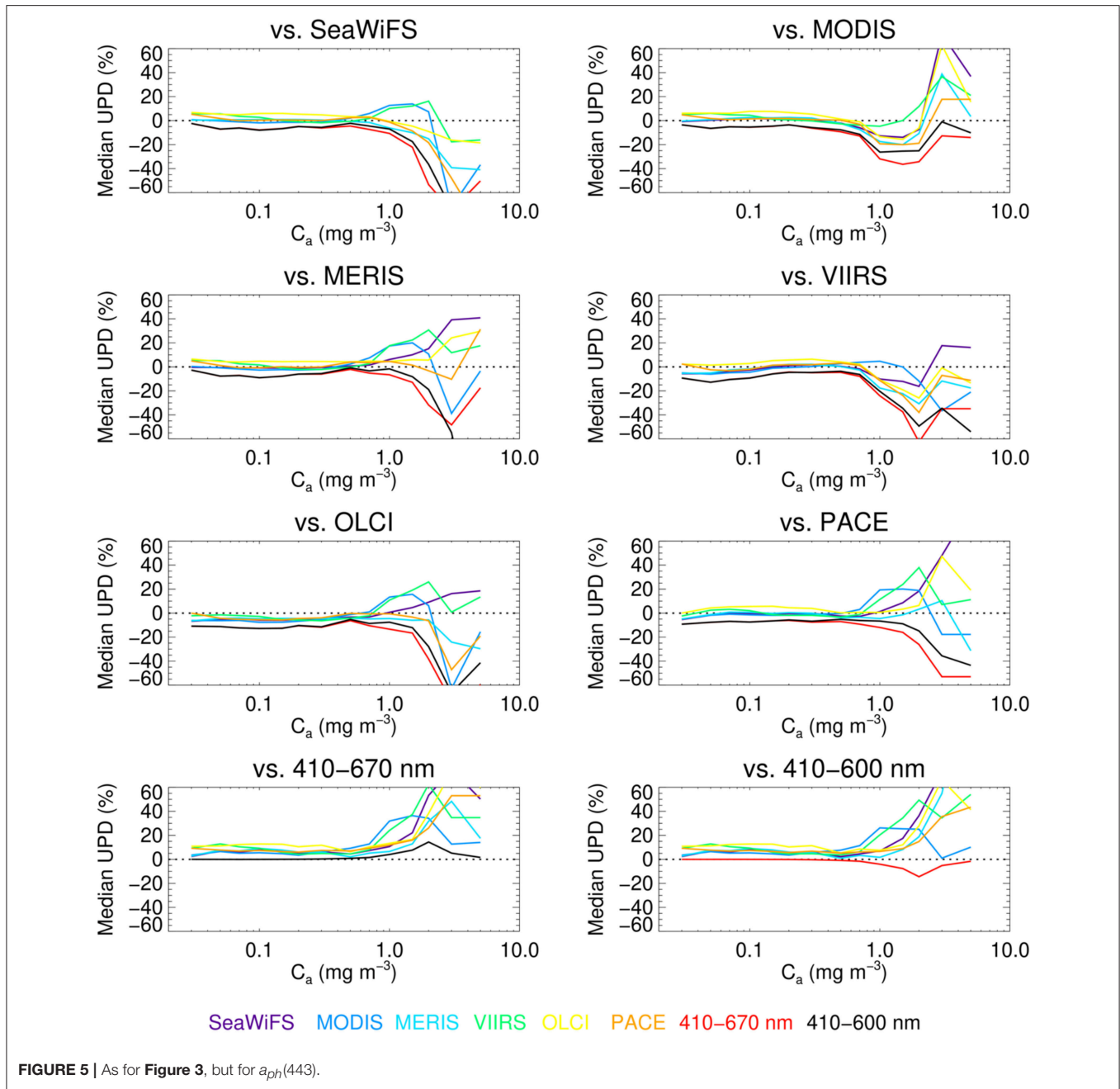**FIGURE 5 |** As for **Figure 3**, but for $a_{ph}(443)$.

to 2.60%, respectively (**Table 3**). These ranges for $a_{dg}(443)$ and $a_{ph}(443)$ generally match those for the oligotrophic C_a range, whereas these ranges for $a(443)$ and $b_{bp}(443)$ compress closer to unity. For comparison, UPDs in $a(555)$, $a_{dg}(555)$, $a_{ph}(555)$, and $b_{bp}(555)$ for SeaWiFS, PACE, and the two 5 nm wavelength suites ranged from -1.50 to 0.21%, -1.74 to 3.99%, -7.47 to 1.34%, and -1.32 to 0.24%, respectively. Generally speaking, the differences between any two wavelength suites remained invariant for $0.1 \leq C_a \leq 0.5$ mg m^{-3}, above which they started to diverge (**Figures 3–6**). SeaWiFS, MODIS, and MERIS differed by ≤ 1.50, 2.32, 0.75, and 2.59% for $a(443)$, $a_{dg}(443)$,

$a_{ph}(443)$, and $b_{bp}(443)$, respectively, in absolute terms. Like the oligotrophic subset, OLCI retrieved low $a_{dg}(443)$ relative to all other wavelength suites. Unlike that subset, however, its $a_{ph}(443)$ retrievals exceeded all other wavelength suites. As for the oligotrophic subset, the two 5 nm wavelength suites retrieved high $a_{dg}(443)$, low $a_{ph}(443)$, and low $b_{bp}(443)$ relative to all other wavelength suites. Their UPD magnitudes, however, fell more in line with the others.

The eutrophic C_a range (capped at 5 mg m^{-3}) realized the most diversity and highest magnitudes in UPDs across all wavelength suites [noting that: (a) SAA retrievals often realize

FIGURE 6 | As for **Figure 3**, but for $b_{bp}(443)$.
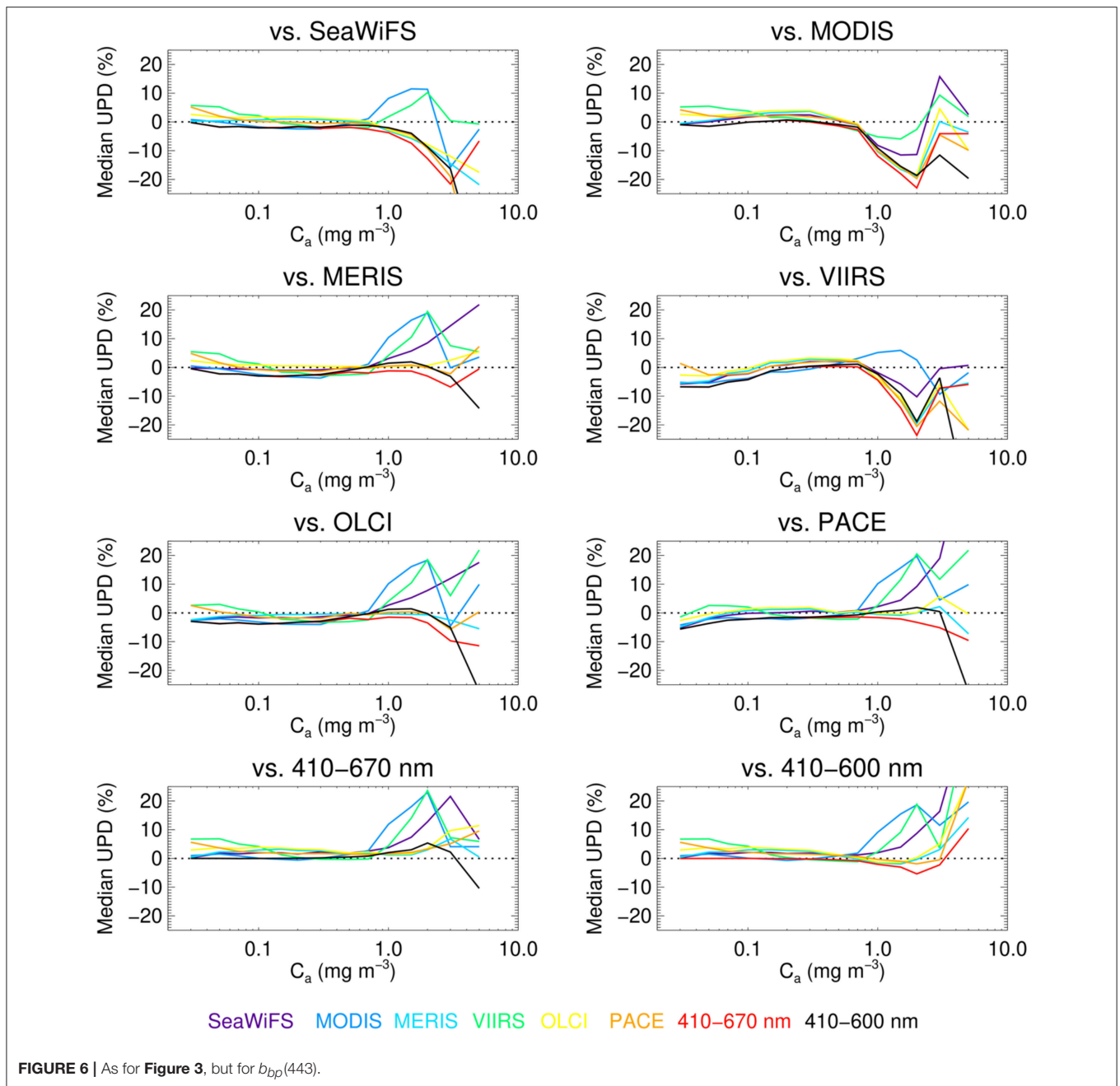
instabilities in such ranges (Werdell et al., 2009, 2018); and (b) the synthesized dataset represents the widest diversity in water in this range [IOCCG, 2006)]. UPDs in $a(443)$, $a_{dg}(443)$, $a_{ph}(443)$, and $b_{bp}(443)$ across all wavelength suites ranged from -16.07 to 12.70%, -19.69 to 17.67%, -53.92 to 12.01%, and -19.50 to 12.99%, respectively (**Table 4**). For comparison, UPDs in $a(555)$, $a_{dg}(555)$, $a_{ph}(555)$, and $b_{bp}(555)$ for SeaWiFS, PACE, and the two 5 nm wavelength suites ranged from -17.00 to 5.33%, -0.24 to 11.23%, -42.26 to 9.31%, and -10.60 to 3.54%, respectively. The differences between any two wavelength suites varied considerably for $C_a > 1$ mg m^{-3} (**Figures 3–6**). Even

SeaWiFS, MODIS, and MERIS differed more substantially than in other C_a ranges—by ≤ 15.74, 15.03, 18.64, and 17.12% for $a(443)$, $a_{dg}(443)$, $a_{ph}(443)$, and $b_{bp}(443)$, respectively, in absolute terms. Like the oligotrophic subset, OLCI retrieved low $a_{dg}(443)$ and high $a_{ph}(443)$ relative to all other wavelength suites, with the exception of MERIS. As for the other two subsets, the two 5 nm wavelength suites retrieved high $a_{dg}(443)$, low $a_{ph}(443)$, and low $b_{bp}(443)$ relative to all other wavelength suites. Their UPDs for $a_{ph}(443)$ far exceeded those for the other suites.

Differences in IOPs from SeaWiFS and SeaWiFS-modified-to-look-like-VIIRS largely demonstrated similar patterns. For

TABLE 2 | Satellite-to-satellite median UPD for IOPs at 443 nm for oligotrophic water ($C_a \leq 0.1$ mg m^{-3}). Relative to Equation (7), columns represent satellite$_1$ and rows represent satellite$_2$ (e.g., MODIS a(443) is 0.49% lower (thus, negative) on average than that for SeaWIFS).

	SeaWiFS	MODIS	MERIS	VIIRS	OLCI	PACE	410–670 nm
a(443)							
MODIS	−0.49						
MERIS	0.30	0.92					
VIIRS	2.30	2.91	2.08				
OLCI	1.41	2.13	1.05	−0.44			
PACE	0.56	1.10	0.35	−1.35	−0.71		
410–670 nm	−1.30	−0.84	−1.76	−3.78	−3.15	−1.97	
410–600 nm	−1.31	−0.88	−1.75	−3.83	−3.15	−1.95	0.00
a_{dg}(443)							
MODIS	−0.40						
MERIS	−0.13	0.28					
VIIRS	0.19	0.60	0.20				
OLCI	−2.61	−2.42	−2.67	−3.14			
PACE	−0.74	0.10	−0.75	−0.62	2.38		
410–670 nm	2.43	2.94	2.55	2.08	5.27	3.13	
410–600 nm	2.43	2.93	2.56	2.08	5.27	3.13	0.00
a_{ph}(443)							
MODIS	−0.42						
MERIS	0.64	1.11					
VIIRS	4.37	5.04	3.50				
OLCI	5.60	6.33	4.82	2.25			
PACE	1.47	2.11	0.89	−1.72	−3.22		
410–670 nm	−5.15	−5.03	−5.99	−9.85	−11.57	−7.46	
410–600 nm	−5.15	−5.14	−6.08	−9.79	−11.56	−7.59	0.01
b_{bp}(443)							
MODIS	−0.75						
MERIS	0.48	1.25					
VIIRS	4.13	4.74	3.55				
OLCI	1.70	2.50	1.15	−1.68			
PACE	1.52	2.21	1.00	−1.65	0.01		
410–670 nm	−1.22	−1.00	−1.64	−6.09	−3.63	−2.99	
410–600 nm	−1.18	−0.94	−1.65	−6.08	−3.61	−2.98	0.01

*Sample sizes follow those presented in **Table 1**.*

context, **Figure 7** shows SeaWiFS-derived C_a (Hu et al., 2012) and the spatial distribution of olig-, meso-, and eutrophic waters, and **Figure 8** shows the SeaWiFS-derived a_{dg}(443), a_{ph}(443), and b_{bp}(443). Naturally, the cumulative distribution of observations falling into each of the trophic levels differs widely in comparison to the synthesized data set, which might be considered in the interpretation of these results. The median SeaWiFS-derived C_a for its olig-, meso-, and eutrophic regions were 0.066, 0.19, and 1.6 mg m^{-3}, respectively. The corresponding median UPDs for a_{dg}(443) for these regions were 1.7, 1.8, and 4.2%, respectively, which approximately track the magnitude of the UPDs at these C_a values in **Figure 4** (upper left panel, green line). Note, however, that VIIRS a_{dg}(443) falls below that for SeaWiFS by ∼2% on average across the synthesized mesotrophic subset. Note also that the mesotrophic subset dominates globally and represents a great diversity in water type (**Figure 7**). The median

UPDs for a_{ph}(443) for the three trophic regions were 9.8, 7.7, and −3.4%, respectively. These also roughly track the UPDs at the corresponding C_a shown in **Figure 5**, with the exception of the eutrophic subset, which also has a sign difference. Finally, the median UPDs for b_{bp}(443) for these regions were 8.9, 8.0, and 2.3%, respectively. These UPDs match those shown in **Figure 6** for the oligo- and eutrophic subsets. Geographically, a_{dg}(443) differ the least between SeaWiFS and surrogate VIIRS, with UPDs that hover around unity (**Figure 8B**). Both a_{ph}(443) and b_{bp}(443) show some latitudinal dependence in their UPDs and surrogate VIIRS-derived values almost unequivocally exceed those from SeaWiFS (**Figures 8D,F**).

As an additional thought experiment to loosely begin to tie our results to marine particle size distributions (PSDs) and, thus, phytoplankton functional types (PFTs), we applied the approach of Hirata et al. (2011) to locate pixels in this SeaWiFS imagery

TABLE 3 | As in Table 2, but for mesotrophic water ($0.1 < C_a \leq 1.0$ mg m^{-3}).

	SeaWiFS	MODIS	MERIS	VIIRS	OLCI	PACE	410–670 nm
$a(443)$							
MODIS	−0.97						
MERIS	0.44	1.50					
VIIRS	−1.09	−0.99	−1.66				
OLCI	0.53	1.37	0.05	1.80			
PACE	−0.69	0.57	−0.58	0.77	−0.67		
410–670 nm	−1.20	−0.36	−1.06	0.07	−1.00	−0.53	
410–600 nm	−0.71	−0.15	−0.57	0.56	−0.74	−0.29	0.22
$a_{dg}(443)$							
MODIS	−1.83						
MERIS	0.50	2.32					
VIIRS	−2.19	0.22	−2.39				
OLCI	−2.79	−1.08	−3.18	−0.94			
PACE	−1.74	0.08	−2.08	0.12	0.79		
410–670 nm	1.82	3.31	1.31	4.01	4.50	3.73	
410–600 nm	1.94	3.31	1.57	4.55	4.79	4.00	0.04
$a_{ph}(443)$							
MODIS	0.75						
MERIS	0.15	−0.50					
VIIRS	−0.25	−1.93	−0.67				
OLCI	4.31	3.11	4.50	4.46			
PACE	1.34	0.31	1.35	1.38	−2.55		
410–670 nm	−6.14	−6.84	−5.13	−6.29	−10.46	−7.37	
410–600 nm	−4.61	−6.50	−4.24	−5.81	−8.95	−6.26	0.45
$b_{bp}(443)$							
MODIS	−1.53						
MERIS	0.65	2.59					
VIIRS	−1.37	−1.08	−2.10				
OLCI	0.94	2.60	0.40	2.45			
PACE	−0.55	1.50	−0.78	1.29	−1.17		
410–670 nm	−2.27	−0.41	−2.18	−0.30	−2.71	−1.66	
410–600 nm	−1.64	−0.18	−1.74	0.00	−2.21	−1.22	0.24

dominated by pico-, nano-, and microplankton (with dominance defined as >50%). On average, SeaWiFS and surrogate VIIRS-derived $a_{dg}(443)$ differed by 1.7, 1.7, and 2.1% for these size classes, whereas $a_{ph}(443)$ and $b_{bp}(443)$ differed by 8.4, 7.6, and 7.8% and 8.0, 7.4, and 8.0%, respectively. These values do not differ substantially from those of the previous exercise as expected, given that Hirata et al. (2011) seeds with C_a, but they offer a modest confirmation of the spatial patterns realized in our analyses. While evaluating the impact of our findings on PSD and PFT retrievals extends beyond the scope of this paper, we feel it remains an obvious follow-on to this work. Many options for estimation of PSDs and PFTs exist and follow-on activities could: (a) build upon our brief example using model-derived distributions of phytoplankton (e.g., Dutkiewicz et al., 2009; Rousseaux and Gregg, 2015); (b) quantify the impacts of varied SAA retrievals within PSD and PFT algorithms that use IOPs as input (see, e.g., IOCCG, 2014; Bracher et al., 2017; Mouw et al., 2017); or; (c) explore in more detail how differences

in SAA retrievals for multiple sensors compare to spectral changes in marine IOPs that occur across natural variations in phytoplankton community composition (Alvain et al., 2012).

Sensitivity of the SAA Parameterization

Our choice in SAA parameterization made little difference in results achieved from the synthesized dataset. **Figures 9–12** follow **Figures 3–6** with the exception that the reported UPDs represent the average for eight SAA parameterizations. At $C_a \leq 0.5$ mg m^{-3}, the patterns in satellite-to-satellite UPDs for the ensemble of runs almost exactly mimicked those for the default SAA runs. This C_a range represents roughly 86% of the retrieved ocean in **Figure 7**. The most obvious difference in UPD patterns emerge at $C_a > 2$ mg m^{-3}, which represents roughly 1.5% of the retrieved ocean. Interestingly, when C_a exceeded 2 mg m^{-3}, UPD values for $b_{bp}(443)$ remained reasonably steady (**Figure 12**) for wavelength suites that included one or more orange/red bands placed between 550 and 670 nm (e.g., 620 nm

TABLE 4 | As in **Table 2**, but for eutrophic water ($1.0 < C_a \leq 5.0\,\text{mg m}^{-3}$).

|	SeaWiFS	MODIS	MERIS	VIIRS	OLCI	PACE	410–670 nm
$a(443)$							
MODIS	9.07						
MERIS	−8.60	−15.74					
VIIRS	6.58	−0.99	12.70				
OLCI	−9.15	−15.84	−0.18	−13.31			
PACE	−8.82	−16.05	−0.92	−13.91	−0.54		
410–670 nm	−8.24	−16.07	−0.36	−13.59	0.08	−0.17	
410–600 nm	−3.43	−12.72	3.12	−9.58	3.54	3.08	3.36
$a_{dg}(443)$							
MODIS	13.14						
MERIS	−2.56	−15.03					
VIIRS	2.79	−10.08	5.70				
OLCI	−8.78	−19.69	−5.85	−10.17			
PACE	−0.03	−13.52	2.04	−3.02	6.58		
410–670 nm	9.53	−2.89	12.17	5.85	17.67	11.65	
410–600 nm	9.62	−3.21	12.44	5.80	17.17	11.23	−0.24
$a_{ph}(443)$							
MODIS	5.88						
MERIS	−18.64	−10.67					
VIIRS	11.83	12.01	23.45				
OLCI	−8.67	−6.21	7.98	−19.08			
PACE	−21.02	−14.05	−3.60	−26.31	−12.40		
410–670 nm	−41.96	−32.87	−28.56	−53.92	−36.99	−25.70	
410–600 nm	−30.47	−22.87	−15.93	−41.08	−21.52	−15.05	9.31
$b_{bp}(443)$							
MODIS	9.33						
MERIS	−9.20	−17.12					
VIIRS	6.34	−2.68	12.99				
OLCI	−8.38	−16.15	0.69	−12.02			
PACE	−8.40	−16.89	−0.47	−13.85	−1.56		
410–670 nm	−10.83	−19.50	−2.85	−15.52	−3.59	−2.58	
410–600 nm	−6.13	−15.51	1.35	−11.57	0.30	1.44	3.54

on MERIS, OLCI, PACE, and the two 5 nm suites). This may be explained, in part, as due to eutrophic $R_{rs}(\lambda)$ spectral features being more distinct in the red and less so in the blue. While differences in SAA retrievals almost certainly increase when directly comparing two parameterizations (vs. comparing one SAA to an ensemble of SAAs), this analysis serves to confirm that our default parameterization sufficiently represents a global average to reinforce that, in general, our results apply universally and do not depend on our choice in SAA parameterization.

DISCUSSION

We set out to use a controlled modeling environment to reveal and quantify the magnitude of change in derived IOPs associated with the use of eight different suites of satellite $R_{rs}(\lambda)$. Ignoring such an analysis as CDRs continue to be developed will result in a prolonged inability to distinguish between algorithmic

and environmental contributions to trends and anomalies in the IOP time-series. We believe we chose a sufficiently robust SAA (and parameterization) to execute this analysis, as we achieved respectable validation results across varied satellite wavelength suites and demonstrated that variations in algorithm parameterization do not affect the final results. Our results ultimately indicated, however, that different suites of satellite $R_{rs}(\lambda)$ do indeed result in divergent IOP retrievals and that these divergences vary with global geography and water type.
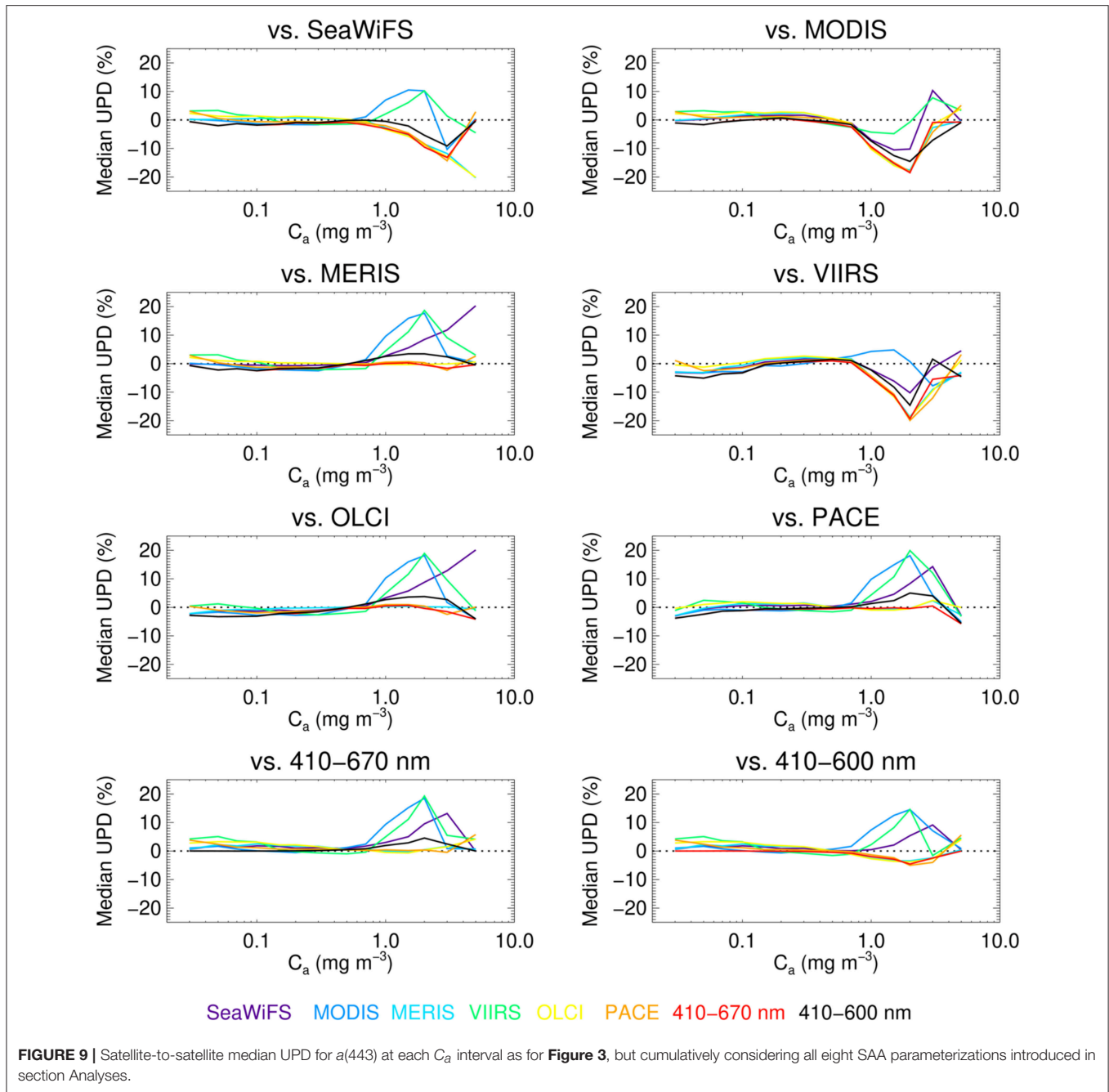
Knowledge of these divergences carries implications and provokes additional questions about remediation strategies and paths forward. A comprehensive evaluation of the implications of our results on trend analyses or CDR development exceeds the scope of this paper. Suffice it to say, however, several of the differences we report will exceed the IOP trends one might wish to reveal, even for sensors with near common wavelengths. These differences will potentially translate into differences in downstream data products (e.g., PSDs, PFTs, and carbon and
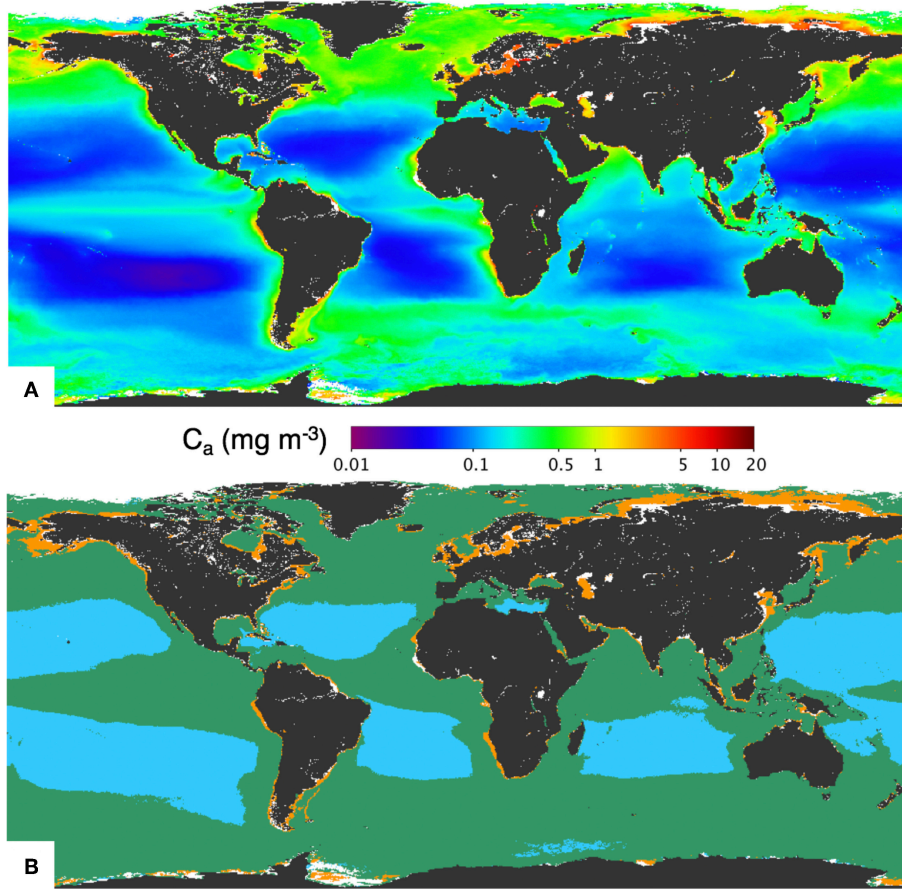
FIGURE 7 | SeaWiFS C_a calculated using mission-long $R_{rs}(\lambda)$ as input into the OCI algorithm (Hu et al., 2012) **(A)** and the global spatial distribution of oligotrophic (cyan), mesotrophic (green), and eutrophic (orange) waters **(B)**. Black and white indicate land and SAA algorithm failure, respectively.
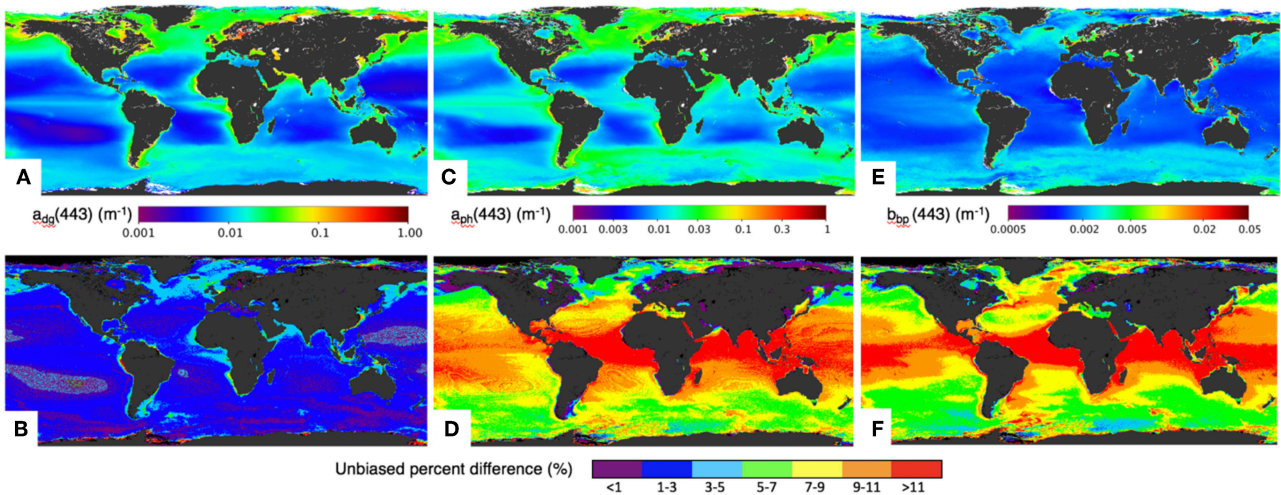

FIGURE 8 | Global IOPs calculated using SeaWiFS mission-long $R_{rs}(\lambda)$ and the UPD between IOP values calculated using SeaWiFS and VIIRS wavelength suites (SeaWIFS = satellite$_1$ and VIIRS = satellite$_2$ in Equation 7). Geophysical values and UPD for $a_{dg}(443)$ shown in **(A,B)**, for $a_{ph}(443)$ in **(C,D)**, and for $b_{bp}(443)$ in **(E,F)**.

FIGURE 9 | Satellite-to-satellite median UPD for $a(443)$ at each C_a interval as for **Figure 3**, but cumulatively considering all eight SAA parameterizations introduced in section Analyses.

primary production data products) that use IOPs as inputs. We devote the remainder of this paper to brief discussions of what we learned, the limitations of our analyses, other confounding issues, and potential remediation strategies that might merit community attention in the future.

As previously stated, we revealed that differences in wavelengths in input $R_{rs}(\lambda)$ lead to several percent differences in derived IOPs when using SAAs (and spectral matching approaches). We contend that this is critical to understand when developing CDRs across satellite platforms. But, we also acknowledge that, while the realized differences occasionally

exceeded several percent, the absolute differences may be small. For example, a 5% window around an absorption value of 0.1 m^{-1} corresponds to $\pm$0.005 m^{-1}, which approaches the detection limit of *in situ* absorption meters. With this in mind, we offer that our results contribute to the knowledge base for CDR development, but should not necessarily be cause for enduring alarm. Perhaps more importantly—at least in the context of identifying needs for future studies—our results also suggest that: (a) validation exercises alone cannot unequivocally identify the differences that will be realized across varied satellite instrument wavelength suites; (b) including 400 nm (in the

FIGURE 10 | As for **Figure 9**, but for $a_{dg}(443)$.
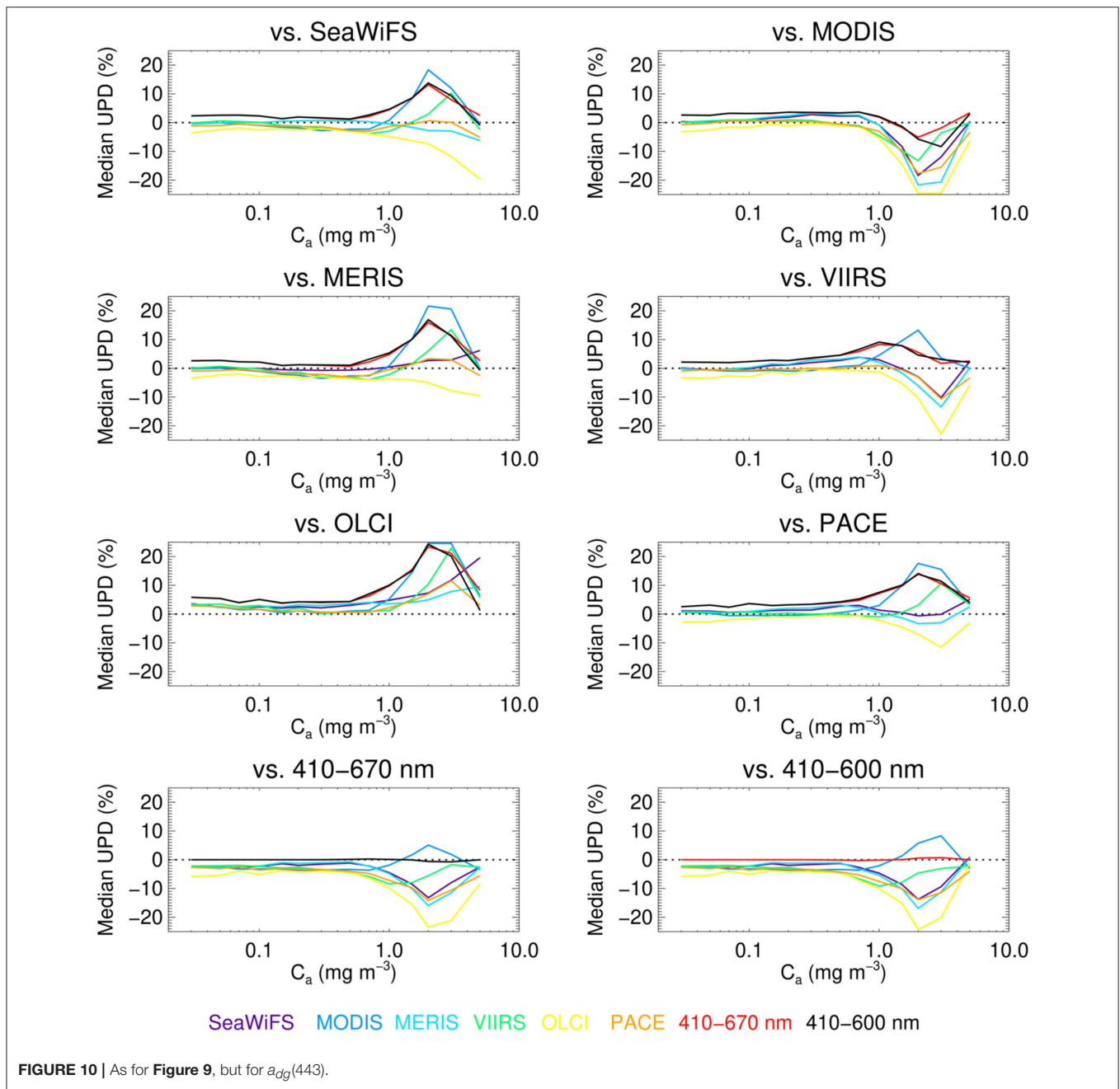
case of OLCI) influences the derived IOPs and UPDs relative to other wavelength suites; (c) using longer wavelengths (> 600 nm) influences the derived IOPs when there is a red signal (e.g., eutrophic conditions); and (d) including additional spectral information shows potential for improved IOP estimation [e.g., those suites with greater spectral resolution reported the lowest combined biases in derived $a_{ph}(443)$ and $b_{bp}(443)$], but not without revisiting SAA parameterizations and execution [e.g., they often also carried the highest biases in derived $a_{dg}(443)$].

What points (b)–(d) above really indicate is the need for additional consideration of SAA behavior as the community

moves toward increased spectral information. This could involve revisiting the use of alternate S_{dg} parameterization when considering additional shorter wavelengths, improved consideration of band-to-band covariances within the inversion strategy, the use of alternate cost functions that exploit additional spectral information (e.g., through weighting or consideration of instrument noise and uncertainties), additional evaluation of the AOP-to-IOP relationship expressed in Equation (2), and the development of schemes that switch between parameterizations under different regions, trophic levels, or bio-optical, hydrological, or environmental conditions, to name

FIGURE 11 | As for **Figure 9**, but for $a_{ph}(443)$.
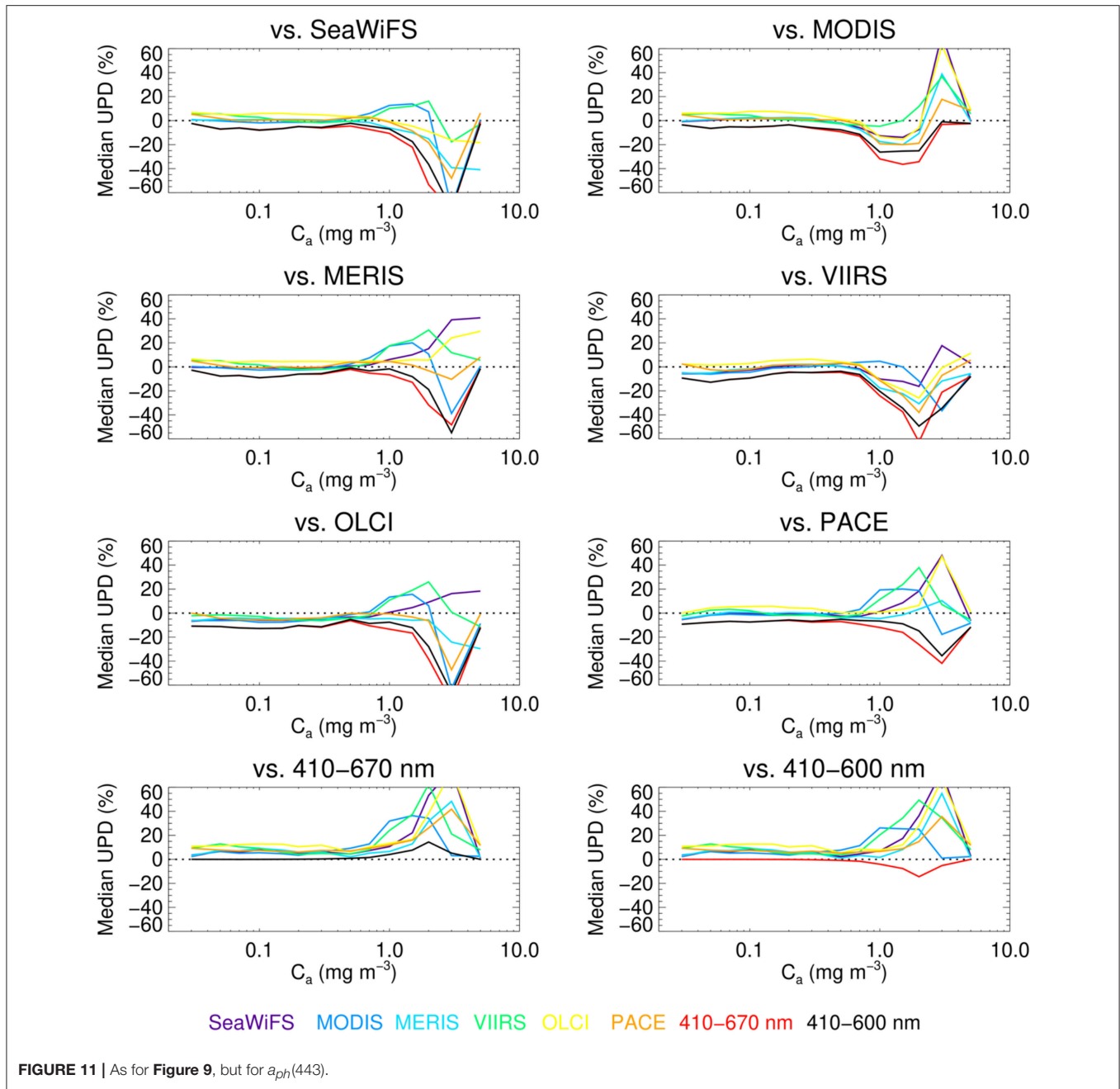
only a few (Werdell et al., 2018). Within the paradigm of CDR development, the need also exists for robust datasets to explore, train, and evaluate SAAs for application to varied satellite instruments.

We considered two independent datasets, but neither perfectly encapsulate or represent all marine conditions at all times. Despite not being perfectly aligned in composition, the two datasets revealed the existence of differences in derived IOPs that generally matched each other in direction and magnitude. Their differences in composition, however, should be considered while interpreting our results. While the synthesized dataset

represents a wide dynamic range of water types, it only represents those conditions that follow its inherent bio-optical assumptions (and, recall, that all bio-optical relationships within this dataset begin with C_a). Note that bio-optical relationships within our SAA differ from those in the synthesized dataset. Furthermore, the cumulative distribution of stations within the synthesized dataset do not numerically represent natural global oligo-, meso-, and eutrophic distributions of seawater. While the mission-long Level-3 SeaWiFS data provided a representation of global distributions of data, they offered long-term averages without explicit consideration of seasonal and geographic variations that

FIGURE 12 | As for **Figure 9**, but for $b_{bp}(443)$.
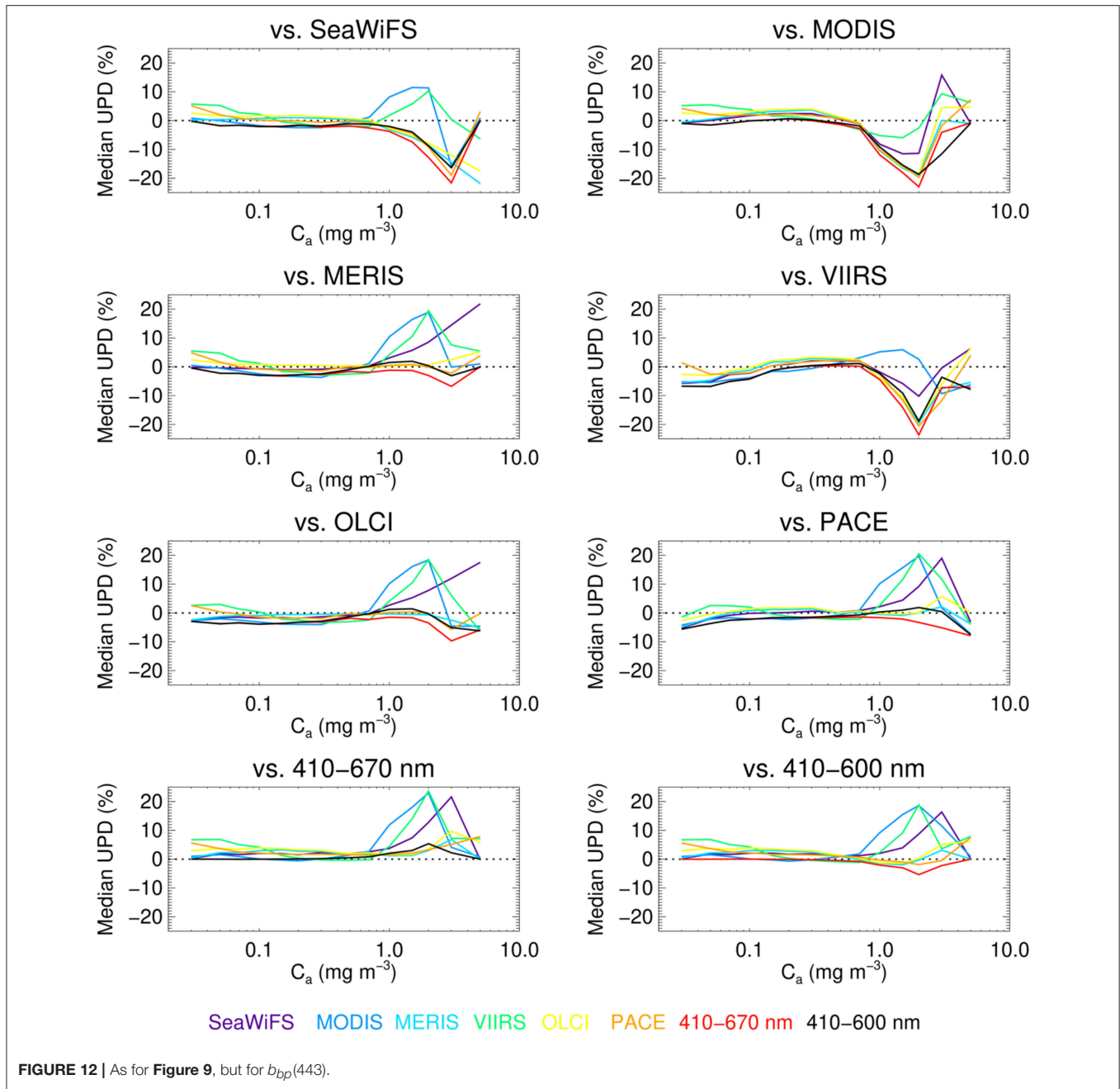
emerge in time-series analyses. All this said, we believe our two datasets adequately complemented each other and offered a broad dynamic range of conditions for this initial study. They successfully indicated similar differences in IOP retrievals, but future results will likely vary depending on the dataset under consideration.

Our analyses used common and consistent input $R_{rs}(\lambda)$ across all eight wavelength suites, which we well known does not represent real life in multi-mission CDR development (e.g., Franz et al., 2005, 2018). Space agencies invest substantial effort into absolute and temporal radiometric characterization

of ocean color satellite instruments that minimizes cross-instrument biases in $R_{rs}(\lambda)$, but differences inevitably remain (Zibordi et al., 2014; Barnes and Hu, 2016; Mélin et al., 2016). Such differences will certainly further confound the compatibility of derived IOPs across satellite instruments, although whether they amplify or dampen our results will vary instrument-to-instrument based on the relative consistencies of the $R_{rs}(\lambda)$. Naturally, relative temporal stability across satellite instruments presents the greatest concern and challenge in long-term CDR development. Other confounding issues include variations in instrument design (e.g., pushbroom vs. whiskbroom and

the resulting number of detectors providing science data), differences in pre-launch instrument characterization activities and methods, differences in protocols and data sources for on-orbit instrument calibration, and variations in algorithms applied prior to executing an SAA, all of which contribute in some way to varied instrument-to-instrument uncertainties in $R_{rs}(\lambda)$.

Once again ignoring the latter for the moment, several proposed strategies exist to mitigate the use of differing $R_{rs}(\lambda)$ as input into bio-optical algorithms. The first, and perhaps least satisfying, simply reduces the number of input wavelengths to the lowest common suite (e.g., limiting SAA execution to roughly 412, 443, 490, 547-555-560, and 667-670-665 nm for MODIS-SeaWiFS-MERIS/OLCI for comparison with VIIRS). Werdell et al. (2009) provides a relevant example of doing so in Chesapeake Bay to retrieve C_a using an SAA. Approaches to shift bands, say from $R_{rs}(547)$ to $R_{rs}(555)$, also exist. Several of the bio-optical algorithms under the OBPG purview, for example, require such adjustment (e.g., Stramski et al., 2008; Hu et al., 2012), which they perform using simple linear statistical relationships developed using *in situ* data (Werdell and Bailey, 2005). Melin and Sclep (2015) developed a more sophisticated band-shifting approach that employs bio-optical models to adjust band centers. Their approach uses preliminary estimates of IOPs such that its use within the context of this analyses would ultimately results in an iterative scheme.

Ultimately, none of these remediation strategies assist with moving from multispectral heritage instruments to future hyperspectral instruments (e.g., PACE). While degrading PACE's spectral resolution to mimic heritage instrumentation remains possible, doing so discards the advances of its instrumentation that we ultimately expect to improve SAA performance and IOP estimation in general, such as inclusion of ultraviolet bands. In the end, this may be unavoidable, with multi-decade IOP-based CDRs in the PACE era reduced to the best available approach across heritage instruments. While we expect novel approaches to emerge that include additional ancillary (environmental) information or spectral weighting/balancing that somewhat mitigate differences in input wavelength suites, the promise of the emerging era of satellite spectroscopy is that additional wavelengths will result in superior data products. Intuitively, we therefore expect two parallel paths forward in

SAA development: one that continues to push the boundary of what is possible with heritage, existing, and planned multispectral instruments (e.g., VIIRS and OLCI) and one that exploits spectroscopy and contiguous spectral resolution. The challenge to the community will then become tracking and understanding differences between the two paths such that the presumably advanced approaches (through spectroscopy) can inform on the underlying limitations and additional uncertainties associated with the long-term (multispectral) data record.

DATA AVAILABILITY

The synthetic dataset generated for this study can be found on PANGAEA (https://doi.pangaea.de/10.1594/PANGAEA. 899407). The satellite imagery can be found on the NASA OceanColor Web site (https://oceancolor.gsfc.nasa.gov).

AUTHOR CONTRIBUTIONS

PW: conceptualization, methodology, and data analysis. LM: synthetic dataset development. PW and LM: original draft, reviewing, editing, and revision.

FUNDING

ACKNOWLEDGMENTS

SUPPLEMENTARY MATERIAL

The Supplementary Material for this article can be found online at: https://www.frontiersin.org/articles/10.3389/feart. 2019.00054/full#supplementary-material

REFERENCES

Alvain, S., Loisel, H., and Dessailly, D. (2012). Theoretical analysis of ocean color radiances anomalies and implications for phytoplankton groups detection in case 1 waters. *Opt. Express* 20, 1070–1083. doi: 10.1364/OE.20.001070

Babin, M., Morel, A., Fournier-Sicre, V., Fell, F., and Stramski, D. (2003). Light scattering properties of marine particles in coastal and open ocean waters as related to the particle mass concentration. *Limnol. Oceanogr.* 48, 843–859. doi: 10.4319/lo.2003.48.2.0843

Barnes, B. B., and Hu, C. (2016). Dependence of satellite ocean color data products on vie wing angles: a comparison between SeaWiFS, MODIS, and VIIRS. *Remote Sens. Environ.* 175, 120–129. doi: 10.1016/j.rse.2015.12.048

Behrenfeld, M. J., Boss, E., Siegel, D. A., and Shea, D. M. (2005). Carbon-based ocean productivity and phytoplankton physiology from space. *Glob. Biogeochem. Cycles* 19:GB1006. doi: 10.1029/2004GB002299

Bracher, A., Bouman, H. A., Brewin, R. J. W., Bricaud, A., Brotas, V., Ciotti, A. M., et al. (2017). Obtaining phytoplankton diversity from ocean color: a scientific roadmap for future development. *Front. Mar. Sci.* 4:e00055. doi: 10.3389/fmars.2017.00055

Brewin, R. J. W., Sathyendranath, S., Muller, D., Brockmann, C., Deschamps, P.-Y., Devred, E., et al. (2015). The Ocean colour climate change initiative: III. A round-robin comparison on in-water bio-optical algorithms. *Remote Sens. Environ.* 162, 271–294. doi: 10.1016/j.rse.2013. 09.016

Bricaud, A., Babin, M., Morel, A., and Claustre, H. (1995). Variability in the chlorophyll-specific absorption coefficients of natural phytoplankton: analysis and parameterization. *J. Geophys. Res.* 100, 13321–13332. doi: 10.1029/95JC00463

Bricaud, A., Morel, A., Babin, M., Allali, K., and Claustre, H. (1998). Variations of light absorption by suspended particles with chlorophyll a concentration

in oceanic (case 1) waters: analysis and implications for bio-optical models. *J. Geophys. Res. Oceans* 103, 31033–31044. doi: 10.1029/98JC02712

Dutkiewicz, S., Follows, M. J., and Bragg, J. G. (2009). Modeling the coupling of ocean ecology and biogeochemistry. *Glob. Biogeochem. Cycles* 23:GB4017. doi: 10.1029/2008GB003405

Eplee, R. E., turpie, K. R., Meister, G., Patt, F. S., Franz, B. A., and Bailey, S.W. (2015). On-orbit calibration of the suomi national polar-orbiting parnership visible infrared imaging radiometer suite for ocean color applications. *Appl. Opt.* 54, 1984–2006. doi: 10.1364/AO.54.001984

Franz, B. A., Karakoylu, E. M., Siegel, D. A., and Westberry, T. K. (2018). Global ocean phytoplankton [in "State of the Climate 2017"]. *Bull. Am. Meteorol. Soc.* 99, S94–S96. doi: 10.1175/2018BAMSStateoftheClimate.1

Franz, B. A., Werdell, P. J., Meister, G., Kwiatkowska, E., Thomas, D., Werdell, J. P., et al. (2005). The continuity of ocean color measurements from SeaWiFS to MODIS. *Proc. SPIE* 58820W. doi: 10.1117/12.620069

Gilerson, A., Ibrahim, A., Foster, R., Carrizo, C., El-Habshi, A., and Ahmed, S. (2014). Retrieval of water optical properties using polarization of light underwater: case I and II waters, *Proc. SPIE* 92400R. doi: 10.1017/12.2067963

Gordon, H. R., Brown, O. B., Evans, R. H., Brown, J. W., Smith, R. C., Baker, K. S., et al. (1988). A Semianalytic Radiance Model of Ocean Color. *J. Geophys. Res.* 93, 10909–10924. doi: 10.1029/JD093iD09p10909

Hirata, T., Hardman-Mountford, N. J., Brewin, R. J. W., Aiken, J., Barlow, R., Suzuki, K., et al. (2011). Synoptic relationships between surface Chlorophyll-a and diagnostic pigments specific to phytoplankton functional types. *Biogeosciences* 8, 311–327. doi: 10.5194/bg-8-311-2011

Hu, C. M., Lee, Z., and Franz, B. (2012). Chlorophyll a algorithms for oligotrophic oceans: a novel approach based on three-band reflectance difference. *J. Geophys. Res. Oceans* 117:C01011. doi: 10.1029/2011jc007395

Ibrahim, A., Gilerson, A., Harmel, T., Tonizzo, A., Chowdhary, J., and Ahmed, S. (2012). The relationship between upwelling underwater polarization and attenuation/absorption ratio. *Opt. Express* 20, 25662–25680. doi: 10.1364/OE.20.025662

IOCCG (2006). *Remote Sensing of Inherent Optical Properties: Fundamentals, Tests of Algorithms, and Applications.* Dartmouth, NS: IOCCG.

IOCCG (2009). *Remote Sensing in Fisheries and Aquaculture.* Dartmouth, NS: IOCCG.

IOCCG (2014). *Phytoplankton Functional Types from Space.* Dartmouth, NS: IOCCG.

IOCCG (2018). *Earth Observations in Support of Global Water Quality Monitoring.* Dartmouth, NS: IOCCG.

Lee, Z. P., Arnone, R., Hu, C. M., Werdell, P. J., and Lubac, B. (2010). Uncertainties of optical parameters and their propagations in an analytical ocean color inversion algorithm. *Appl. Opt.* 49, 369–381. doi: 10.1364/AO.49.000369

Lee, Z. P., Carder, K., Arnone, R., and He, M. X. (2007). Determination of primary spectral bands for remote sensing of aquatic environments. *Sensors* 7, 3428–3441. doi: 10.3390/s7123428

Lee, Z. P., Carder, K. L., and Arnone, R. A. (2002). Deriving inherent optical properties from water color: a multiband quasi-analytical algorithm for optically deep waters. *Appl. Opt.* 41, 5755–5772. doi: 10.1364/AO.41.005755

Lee, Z. P., Carder, K. L., and Du, K. P. (2004). Effects of molecular and particle scatterings on the model parameter for remote-sensing reflectance. *Appl. Opt.* 43, 4957–4964. doi: 10.1364/AO.43.004957

Lee, Z. P., Carder, K. L., Hawes, S. K., Steward, R. G., Peacock, T. G., and Davis, C. O. (1994). Model for the interpretation of hyperspectral remote-sensing reflectance. *Appl. Opt.* 33, 5721–5732. doi: 10.1364/AO.33.005721

Lee, Z. P., Du, K. P., Voss, K. J., Zibordi, G., Lubac, B., Arnone, R., and Weidemann, A. (2011). An inherent-optical-property-centered approach to correct the angular effects in water-leaving radiance. *Appl. Opt.* 50, 3155–3167. doi: 10.1364/AO.50.003155

Loisel, H., Stramski, D., Dessailly, D., Jamet, C., Li, L., and Reynolds, R. A. (2018). An inverse model for estimating the optical absorption and backscattering coefficients of seawater from remote-sensing reflectance over a broad range of oceanic and coastal marine environments. *J. Geophys. Res.* 123, 2141–2171. doi: 10.1002/2017JC013632

Maritorena, S., d'Andon, O. H. F., Mangin, A., and Siegel, D. A. (2010). Merged satellite ocean color data products using a bio-optical model: characteristics, benefits and issues. *Remote Sens. Environ.* 114, 1791–1804. doi: 10.1016/j.rse.2010.04.002

McKinna, L. I. W., Werdell, P. J., and Proctor, C. W. (2016). Implementation of an analytical Raman scattering correction for satellite ocean-color processing. *Opt. Express* 24, A1123–1137. doi: 10.1364/OE.24.0A1123

Meister, G., and Franz, B. A. (2014). Corrections to the MODIS Aqua calibration derived from MODIS Aqua ocean color products. *IEEE Trans. Geosci. Remote Sens.* 52, 6534–6541. doi: 10.1109/TGRS.2013.2297233

Meister, G., Franz, B. A., Kwiatkowska, E. J., and McClain, C. R. (2012). Corrections to the calibration of MODIS Aqua Ocean color bands derived from SeaWiFS data. *IEEE Trans. Geosci. Remote Sens.* 50, 310–319. doi: 10.1109/TGRS.2011.2160552

Melin, F., and Sclep, G. (2015). Band shifting for ocean color multi-spectral reflectance data. *Opt. Express* 23, 2262–2279. doi: 10.1364/OE.23.002262

Mélin, F., Sclep, G., Jackson, T., and Sathyendranath, S. (2016). Uncertainty estimates of remote sensing reflectance derived from comparison of ocean color satellite data sets. *Remote Sens. Environ.* 177, 107–124. doi: 10.1016/j.rse.2016.02.014

Mobley, C. D., and Sundman, L. K. (2008). *Hydrolight 5 Ecolight 5.* Washington, DC: Sequoia Scientific Inc.

Mobley, C. D., Werdell, J., Franz, B., Ahmad, Z., and Bailey, S. (2016). *Atmospheric Correction for Satellite Ocean Color Radiometry.* NASA Technical Memorandum, NASA/TM-2016-217551, 85.

Mouw, C. B., Hardman-Mountford, N. J., Alvain, S., Bracher, A., Brewin, R. J. W., Bricaud, A., et al. (2017). A consumer's guide to satellite remote sensing of multiple phytoplankton groups in the global ocean. *Front. Mar. Sci.* 4:41. doi: 10.3389/fmars.2017.00041

NRC (2004). *Climate Data Records From Environmental Satellites: Interim Report.* Washington, DC: National Academies Press.

NRC (2011). *Assessing Requirements for Sustained Ocean Color Research and Operations.* Washington, DC: National Academies Press.

O'Reilly, J. E., Maritorena, S., Mitchell, B. G., Siegel, D. A., Carder, K. L., Garver, S. A., et al. (1998). Ocean color chlorophyll algorithms for SeaWiFS. *J. Geophys. Res.* 103, 24937–24953. doi: 10.1029/98JC02160

PACE Science Definition Team (2018). *Pre-Aerosols, Clouds, and Ocean Ecosystem (PACE) Mission Science Definition Team Report.* PACE Technical Report Series, NASA/TM-2018-219027/Vol. 2, 316.

Patt, F. S., Barnes, R. A., Eplee, R. E. Jr, Franz, B. A., Robinson, W. D., et al. (2003). "Algorithm updates for the fourth seawifs data reprocessing," in *Goddard Space Flight Center*, eds S. B. Hooker and E. R. Firestone (Greenbelt, MD: National Aeronautics and Space Administration), 74.

Pope, R. M., and Fry, E. S. (1997). Absorption spectrum (380-700 nm) of pure water. II. Integrating cavity measurements. *Appl. Opt.* 36, 8710–8723. doi: 10.1364/AO.36.008710

Roesler, C., Perry, M. J., and Carder, K. L. (1989). Modeling *In-situ* phytoplankton absorption from total absorption-spectra in productive inland marine waters. *Limnol. Oceanogr.* 34, 1510–1523. doi: 10.4319/lo.1989.34.8.1510

Rousseaux, C. S., and Gregg, W. W. (2015). Recent decadal trends in global phytoplankton composition. *Glob. Biogeochem. Cycles* 29, 1674–1688. doi: 10.1002/2015GB005139

Sathyendranath, S., Brewin, R. J. W., Jackson, T., Melin, F., and Platt, T. (2017). Ocean-colour products for climate-change studies: what are their ideal characteristics? *Remote Sens. Environ.* 203, 125–138. doi: 10.1016/j.rse.2017.04.017

Siegel, D. A., Behrenfeld, M., Maritorena, S., McClain, C. R., Antoine, D., Bailey, S. W., et al. (2013). Regional to global assessments of phytoplankton dynamics from the SeaWiFS mission. *Remote Sens. Environ.* 135, 77–91. doi: 10.1016/j.rse.2013.03.025

Siegel, D. A., Buesseler, K. O., Doney, S. C., Sailley, S. F., Behrenfeld, M. J., and Boyd, P. W. (2014). Global assessment of ocean carbon export by combining satellite observations and food-web models. *Glob. Biogeochem. Cycles* 28, 181–196. doi: 10.1002/2013GB004743

Stramski, D., Boss, E., Bogucki, D. J., and Voss, K. J. (2004). The role of seawater constituents in light backscattering in the ocean. *Progr. Oceanogr.* 61, 27–56. doi: 10.1016/j.pocean.2004.07.001

Stramski, D., Reynolds, R. A., Babin, M., Kaczmarek, S., Lewis, M. R., Rottgers, R., et al. (2008). Relationships between the surface concentration of particulate organic carbon and optical properties in the eastern South Pacific and eastern Atlantic Oceans. *Biogeosciences* 5, 171–201. doi: 10.5194/bg-5-171-2008

Twardowski, M. S., Boss, E., Sullivan, J. M., and Donaghay, P. L. (2004). Modeling the spectral shape of absorption by chromophoric dissolved organic matter. *Mar. Chem.* 89, 69–88. doi: 10.1016/j.marchem.2004.02.008

Vandermuelen, R. A., Mannino, A., Neeley, A. R., Werdell, P. J., and Arnone, R. (2017). Determining the optimal spectral sampling frequency and uncertainty thresholds for hyperspectral remote sensing of ocean color. *Opt. Express* 25, A785–A797. doi: 10.1364/OE.25.00A785

Wang, M., Franz, B. A., Barnes, R. A., and McClain, C. R. (2001). Effects of spectral bandpass on SeaWiFS-retrieved near-surface optical properties of the ocean. *Appl. Opt.* 40, 343–348. doi: 10.1364/AO.40.000343

Werdell, P. J., and Bailey, S. W. (2005). An improved *in-situ* bio-optical data set for ocean color algorithm development and satellite data product validation. *Remote Sens. Environ.* 98, 122–140. doi: 10.1016/j.rse.2005.07.001

Werdell, P. J., Bailey, S. W., Franz, B. A., Harding, L. W. Jr, Feldman, G. C., and McClain, C. R. (2009). Regional and seasonal variability of chlorophyll-a in Chesapeake Bay as observed by SeaWiFS and MODIS-Aqua. *Remote Sens. Environ.* 113, 1319–1330. doi: 10.1016/j.rse.2009.02.012

Werdell, P. J., Franz, B. A., Bailey, S. W., Feldman, G. C., Boss, E., Brando, V. E., et al. (2013a). Generalized ocean color inversion model for retrieving marine inherent optical properties. *Appl. Opt.* 52, 2019–2037. doi: 10.1364/AO.52.002019

Werdell, P. J., Franz, B. A., Lefler, J. T., Robinson, W. D., and Boss, E. (2013b). Retrieving marine inherent optical properties from satellites using temperature and salinity-dependent backscattering by seawater. *Opt. Express* 21, 32611–32622. doi: 10.1364/OE.21.032611

Werdell, P. J., McKinna, L. I. W., Boss, E., Ackleson, S. G., Craig, S. E., Gregg, W. W., et al. (2018). An overview of approaches and challenges for retrieving marine inherent optical properties from ocean color remote sensing. *Progr. Oceanogr.* 160, 186–212. doi: 10.1016/j.pocean.2018.01.001

Werdell, P. J., Roesler, C. S., and Goes, J. I. (2014). Discrimination of phytoplankton functional groups using an ocean reflectance inversion model. *Appl. Opt.* 53, 4833–4849. doi: 10.1364/AO.53.004833

Westberry, T. K., Boss, E., and Lee, Z. (2013). Influence of Raman scattering on ocean color inversion models. *Appl. Opt.* 52, 5552–5561. doi: 10.1364/AO.52.005552

Wolanin, A., Soppa, M. A., and Bracher, A. (2016). Investigation of spectral band requirements for improving retrievals of phytoplankton functional types. *Remote Sens.* 8:871. doi: 10.3390/rs8100871

Zhang, X. D., Hu, L. B., and He, M. X. (2009). Scattering by pure seawater: effect of salinity. *Opt. Express* 17, 5698–5710. doi: 10.1364/OE.17.005698

Zheng, G. M., and Stramski, D. (2013). A model based on stacked-constraints approach for partitioning the light absorption coefficient of seawater into phytoplankton and non-phytoplankton components. *J. Geophys. Res.* 118, 2155–2174. doi: 10.1002/jgrc.20115

Zibordi, G., Donlon, C., and Parr, A. (2014). *Optical Radiometry for Ocean Climate Measurements*. Academic Press.